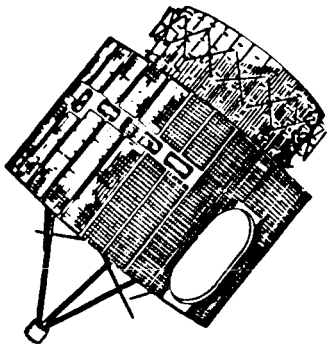


REPORT NO. 83HVO02
JUNE 1987

PREPARED UNDER
NASA/MSFC CONTRACT
NO. NAS8-34596

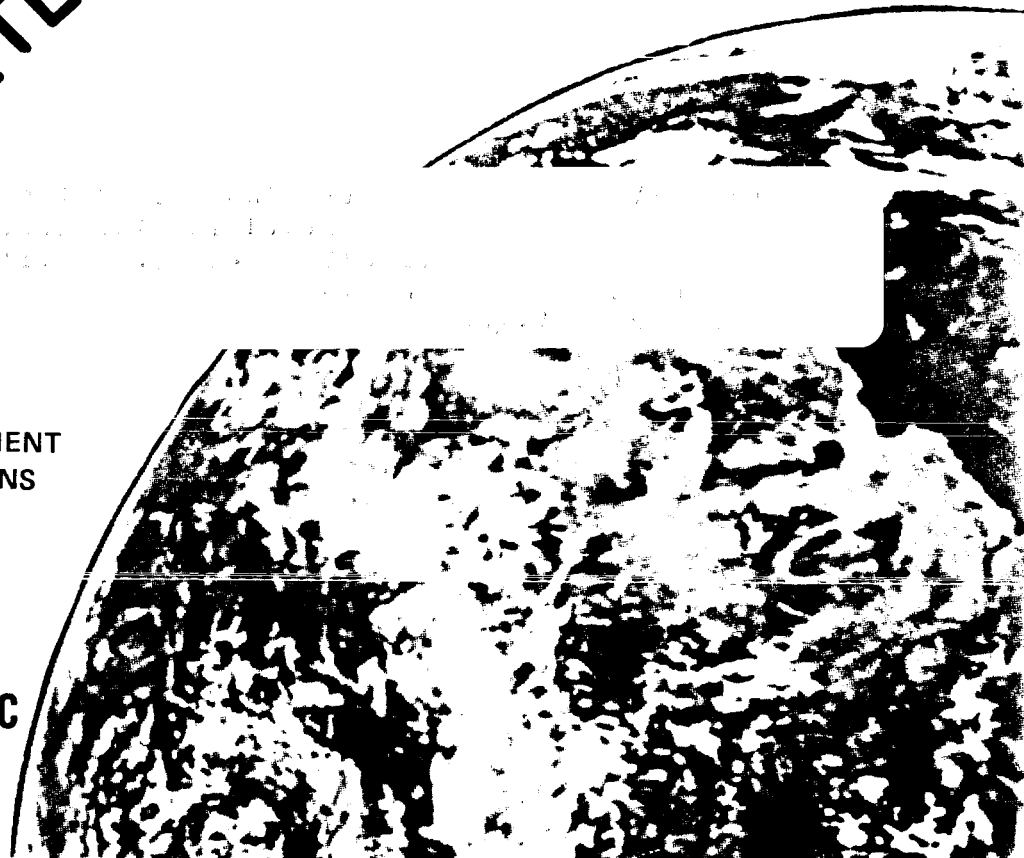
FINAL REPORT



AUTOMATED MESOSCALE WINDS DETERMINED FROM SATELLITE IMAGERY

PREPARED BY
GENERAL ELECTRIC COMPANY
AUTOMATED SYSTEMS DEPARTMENT
HUNTSVILLE CENTER OPERATIONS
HUNTSVILLE, ALABAMA

GENERAL  ELECTRIC



REPORT NO. 83HV002
JUNE 1987

FINAL REPORT

AUTOMATED MESOSCALE WINDS
DETERMINED FROM
SATELLITE IMAGERY

PREPARED UNDER
NASA/MSFC CONTRACT
NO. NAS8-34596

R. J. ATKINSON
Study Program Manager

GENERAL ELECTRIC COMPANY
AUTOMATED SYSTEMS DEPARTMENT
HUNTSVILLE, ALABAMA

TABLE OF CONTENTS

SECTION/ PARAGRAPH	TITLE	PAGE
1.	INTRODUCTION	1
2.	PREPROCESSING OF GOES IMAGERY	3
2.1	Registration of Image Sequences with respect to the Earth	3
2.2	Resample the Infrared Imagery to Visible Scene Resolution	3
2.3	Registration of Infrared Scenes to Visible Data Scenes	6
2.4	Preprocessing of Data for Noise Removal	6
2.5	Filtering of Visible Data for Enhancement	8
2.5.1	One Dimensional Derivative or Slope Filter	8
2.5.2	Sobel Filter	10
2.5.3	Scene Brightness	10
2.5.4	Edge Preserving Filter	10
3.	CLOUD TRACKING TECHNIQUE	13
3.1	Filtering of Visible Image Data	14
3.2	Candidate Cloud Template Positions	20
3.3	Template Size	20
3.4	Search Area Size	25
3.5	Motion Vector Quality Control	25
3.7	Height Determination	33
3.6	Image Acquisition Time Separation	33
4.	STRUCTURAL AND KINEMATIC ANALYSIS OF AUTOMATED WINDS	37
4.1	The 24 April 1975 (AVE IV) Case Study	37
4.2	Manual and Automated Wind Vectors	37
4.3	Mesoscale Analysis	37
4.4	Structure Functions	41
5.	VISSR ATMOSPHERIC SOUNDER (VAS) DATA	43
5.1	Preprocessing of VAS Data	43
5.1.1	Equalization of Means and Variances	43
5.1.2	Histogram Equalization	45
5.1.3	Mean Value Filtering	45
5.2	Water Vapor Winds	45
6.	CONCLUSIONS	49
7.	REFERENCES	50

LIST OF ILLUSTRATIONS

FIGURE	TITLE	PAGE
2-1.	Full resolution visible test image	4
2-2.	Visible test image of 1024 X 1024 pixels	5
2-3.	Example of IR image magnified to visible resolution ..	7
2-4.	Gradient filtered image	9
2-5.	Sobel filter output	11
2-6.	Edge Preserving filtered image	12
3-1.	Displacement results using raw data input	15
3-2.	Displacement results using gradient filtered input....	16
3-3.	Displacement results using Sobel filtered input	17
3-4.	Displacement results using scene brightness input	18
3-5.	Effects of preprocessing on motion vector consistency	19
3-6.	Standard deviation image	21
3-7.	Results obtained with a 7 X 7 template	22
3-8.	Results obtained with a 21 X 21 template	23
3-9.	Effects of template size on motion vector consistency	24
3-10.	Example of wind vectors placed on a grid	22
3-11.	Low level satellite derived and RAOB winds	28
3-12.	Winds from edge preserving filter input	29
3-13.	Winds from Sobel filter combined with raw data	30
3-14.	Winds from Sobel filter values as input	31
3-15.	Winds from compass filter as input	32
3-16.	Motion vectors including upper level winds	34
3-17.	Winds from images separated by 10 minutes	35
3-18.	Winds from images separated by 15 minutes	36
4-1.	Automated low-level winds superimposed on the visible image	38
4-2.	Manual and automated wind vectors	39
4-3.	Low-level divergence computed from automated winds ...	40
4-4.	Structure function plots of the u and v components ...	42
5-1.	Standard VAS weighting functions	44
5-2.	Results of line interpolation on VAS imagery	46
5-3.	Automated water vapor winds superimposed on VAS water vapor imagery	47
5-4.	Gridded RAOB winds superimposed on VAS imagery	48

1. INTRODUCTION

In the 1960s, cloud movements observed in visible ATS images were used to demonstrate that estimation of tropospheric winds from satellite data was possible. Subsequently in the 1970s, these satellite-derived cloud winds were operationally derived on global and synoptic scales using visible and infrared imagery from the GOES spacecraft. A review article by Hubert (1979) describes large-scale cloud wind research accomplishments and operational systems that are currently in use.

The SMS/GOES visible imagery was used to demonstrate the importance of mesoscale systems in creating local weather variability and initiating severe storms. The ability to manually extract wind fields and obtain derived kinematic quantities was demonstrated by several investigators (Negri and Vonder Haar, 1980, Maddox and Vonder Haar, 1979, Wilson and Houghton, 1979, Rodgers et al, 1979, Pelsen, 1980, and others). However, these mesoscale measurements are difficult and time-consuming to produce and are not presently available on an operational basis.

The purpose of this report is to describe a new multispectral image-processing system for extracting mesoscale wind fields automatically from sequences of GOES imagery. This system is unique for many reasons including:

1. no limitation on the computational power required for system execution was used as a constraint on system design,
2. a new pattern recognition technique was used, incorporating objective selection of template locations and sizes,
3. the system is multispectral in design so that both visible and infrared data are required and water vapor tracking and CO₂-slicing cloud height assignments may be an integral part of the final system,
4. wind vectors are generated at mesoscale resolution in space (~10 km spacing),
5. quality control is done objectively based upon image processing parameters requiring less than 1% of the computed winds to be edited by objective or subjective meteorological procedures and
6. near real-time (within 1 hour) mesoscale wind fields can be generated for research or operational evaluations over a 512 X 512 image using super minicomputers with array processors. (less than 1 minute of class 6 computer time is required for real-time purposes when the computer code is vectorized.)

This system was developed using GOES five-minute imagery acquired on April 24, 1975, from which several investigators have manually computed and extensively analyzed cloud wind estimates. Structural and kinematic analyses of the automated vs manual winds are performed to demonstrate that the automated wind estimates have an overall statistical error smaller than the manual winds and produce spatially and temporally consistent results down to the small meso-B scale in numerous pre-thunderstorm areas. The tracking system was also applied to VISSR Atmospheric Sounder (VAS) measurements in the H2O absorption bands.

2. PREPROCESSING OF GOES IMAGERY

The initial investigations were performed on a 200 X 200 pixel area acquired April 24, 1975, shown in figure 2-1. The cloud band in the upper section of this scene follows the Gulf coast. Several functions were performed on the GOES full resolution image sequences before computing wind estimates. These are described in the following paragraphs.

2.1 Registration of Image Sequences with Respect to the Earth

The imaging instrument on GOES is the VISSR (Visible-Infrared Spin Scan Radiometer). An image is formed by the VISSR scanning the earth, west to east, as the satellite spins. Electronic sampling generates equal angle (or time) spacing between successive image elements on each scan line. After each spin, a scan mirror is stepped down so that the next scan sweep is slightly south of the previous sweep. The ground coverage of successive images varies because of anomalies in the spacecraft orbit and attitude. The GOES orbit is not perfectly circular and it is slightly inclined to the equatorial plane, and is perturbed by anomalies in the earth's gravitational force field, the gravitational effect of the Moon and the Sun, and the pressure of the solar wind. Departure from an ideal geosynchronous orbit causes the satellite subpoint to trace out a distorted figure eight during its one-day orbital period.

A set of orbit parameters determines the satellite's position and a set of attitude parameters determines the orientation of the satellite's spin axis relative to the Earth as functions of time. The algorithms for navigating geosynchronous satellite images use the positions of recognizable stars and Earth-based landmarks measured in image frames to determine the attitude, the misalignment angles, and the orbit parameters. The computer programs required for transforming between satellite image coordinates (pixel row and column number) and Earth coordinates (latitude and longitude) were obtained from the University of Wisconsin. Also, acquired were the navigation parameters valid for April 24, 1975 from 1800 GMT to 2400 GMT. By using the navigation transformations, larger test images of 1024 by 1024 pixels (figure 2-2) were extracted and centered at an earth location which was chosen as coordinates 37° N, 97° W (on the Kansas-Oklahoma border).

2.2 Resampling of Infrared Imagery to Visible Scene Resolution

Resampling is a form of interpolation and consists of constructing a data point from adjacent points. A suitable resampling algorithm is a four-point approximation of a $(\sin x)/x$ function. Assume the point to be resampled lies between two points in a regularly spaced linear array, e.g., an input scan line, and let D be the distance from the preceding array point. The intensity value can be determined from the intensities of four neighboring points in the array as follows:

$$I = D^3 (-I_1 + I_2 - I_3 + I_4) + D^2 (2I_1 - 2I_2 + I_3 - I_4) + D (-I_1 + I_3) + I_2$$

ORIGINAL PAGE IS
OF POOR QUALITY

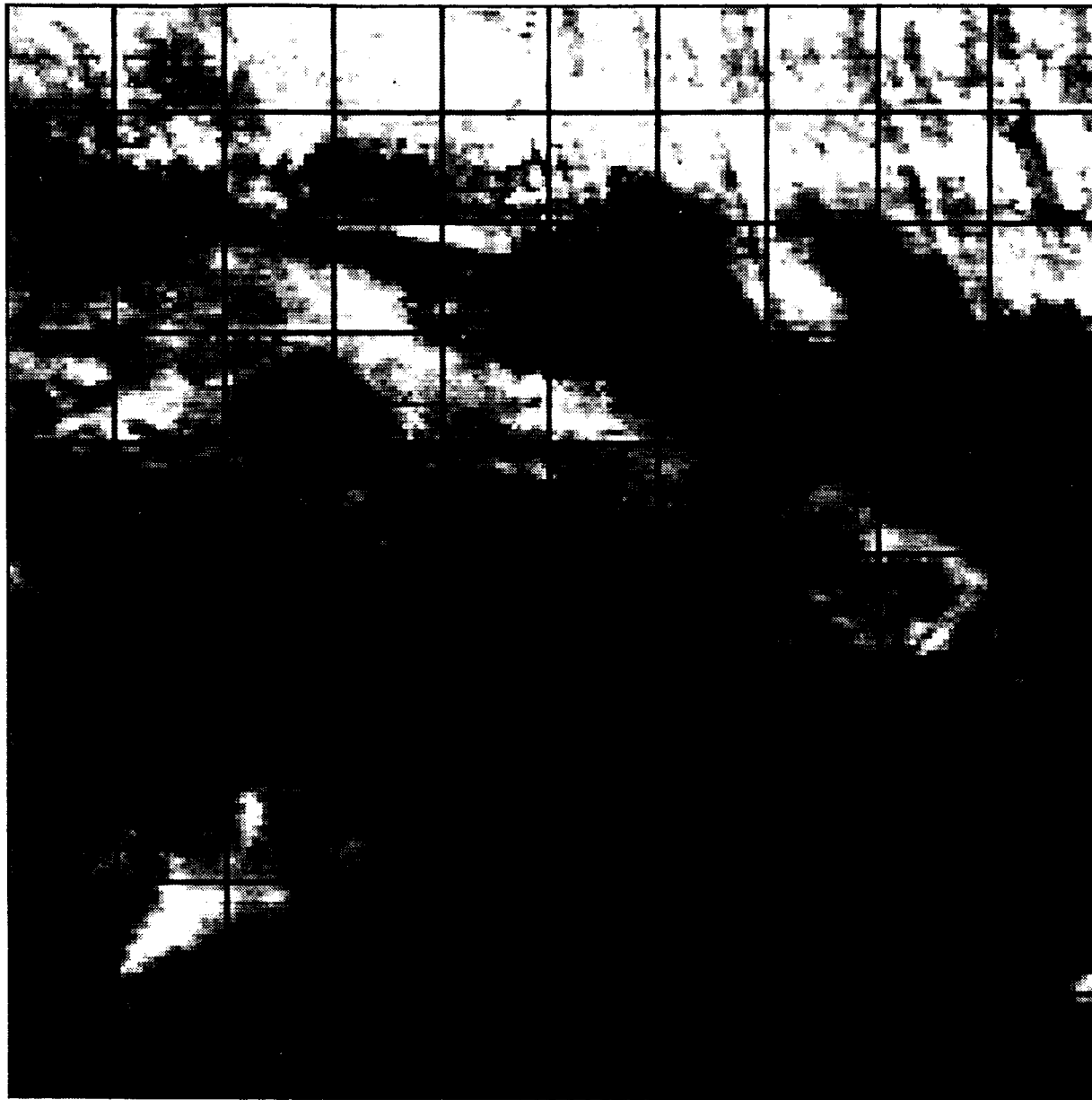


Figure 2-1. Full resolution visible test image

ORIGINAL PAGE IS
OF POOR QUALITY

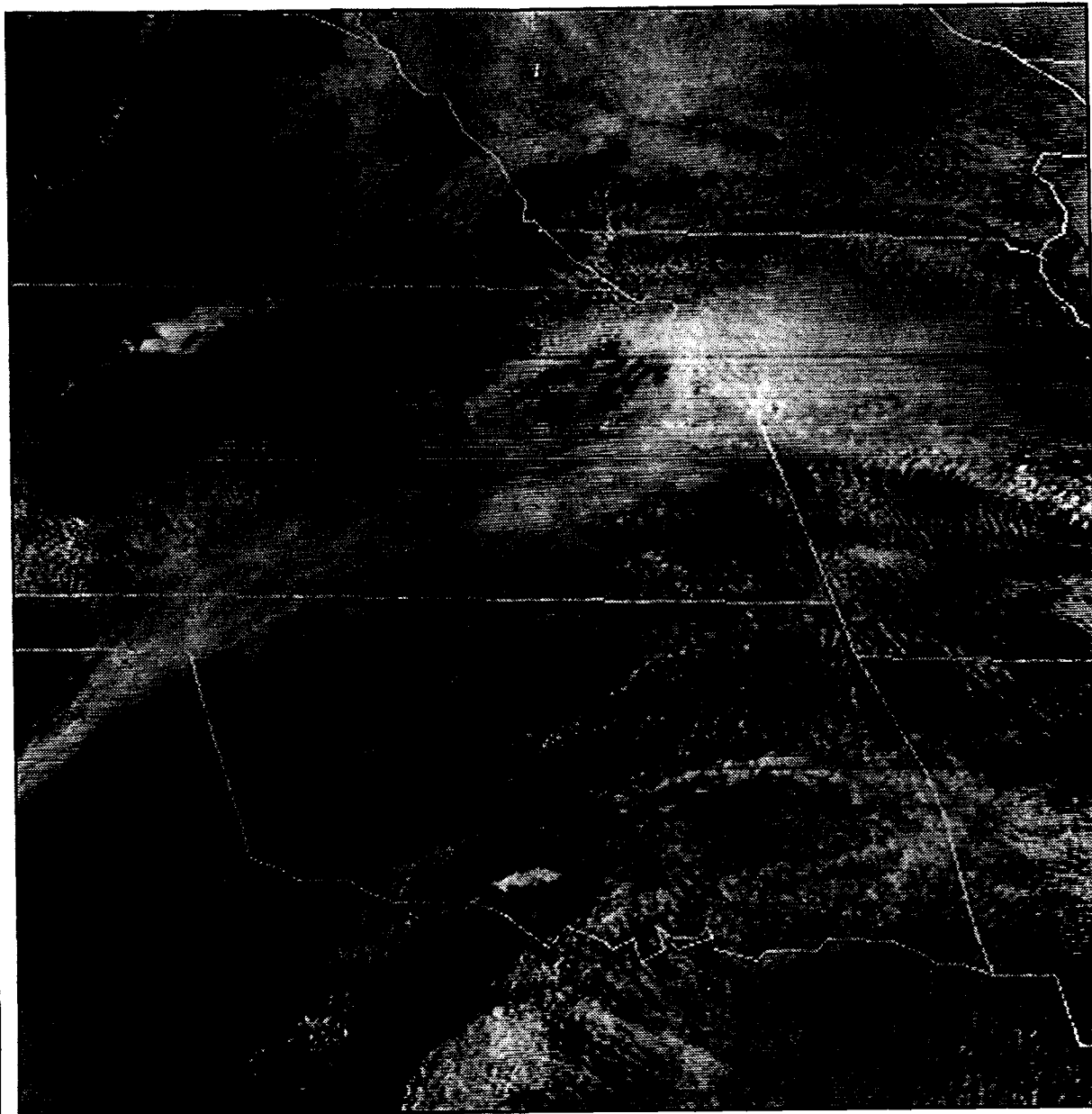


Figure 2-2. Visible test image of 1024 by 1024 pixels

Thus, it is necessary to include four points in a computation of the pixel value to be placed in the corrected image. By inserting multiple points, the image can be magnified. In order to magnify the infrared imagery to the visible image resolution, the magnification factor must be four along scan lines, and eight across scan lines. Thus, the output pixel coordinates are multiples of four or eight. However, output pixels can be skipped to allow for the exact infrared image starting coordinates after magnification. An example of a magnified IR image is given in figure 2-3.

2.3. Registration of Infrared Scenes to Visible Data Scenes

The eight visible data records produced during each spacecraft rotation correspond to one infrared sensor line but with eight times the resolution. Along the scan lines, the visible resolution is four times, resulting in a visible resolution of about 1 kilometer by 1 kilometer and an infrared resolution of 8 kilometers by 4 kilometers.

The sensor was designed so that visible and infrared picture data would be generated concurrently by the spacecraft. However, when examining concurrent infrared images which had been magnified to the visible data resolution, it became apparent that the infrared scene was shifted by several elements to the east. The change in sensor characteristics has been attributed to launch vibration.

The number of pixels in the infrared scene shift was determined by finding the displacement of the infrared scene with respect to the visual scene data obtained at the same time. The cloud motion program with a template size of 125 by 125 pixels was used. The infrared scene was expanded to visible scene resolution by cubic interpolation.

The majority of the measured shifts occurred near 16 pixels. The average of the 1273 shifts obtained in the range 11 to 21 was 15.8 pixels. The value of 16 pixels for this sensor has been verified by visual examination of several image sets at the University of Wisconsin (Wylie, 1980).

2.4 Preprocessing of Data for Noise Removal

The infrared thermal detectors are subject to the insertion of noise in the data values which form the imagery. These incorrect values may appear as a mis-calibrated or noisy scan line, or at isolated pixel locations. They are unacceptable because of the use of infrared pixel values to determine template temperatures. Visible imagery suffers from occasional noisy scan lines.

Scan lines which are to be corrected were determined manually by displaying the imagery. The data values in these records were then replaced by the averages of the pixel values in their nearest neighbor records. This procedure was also followed when more than one adjacent record was to be replaced.

ORIGINAL PAGE IS
OF POOR QUALITY

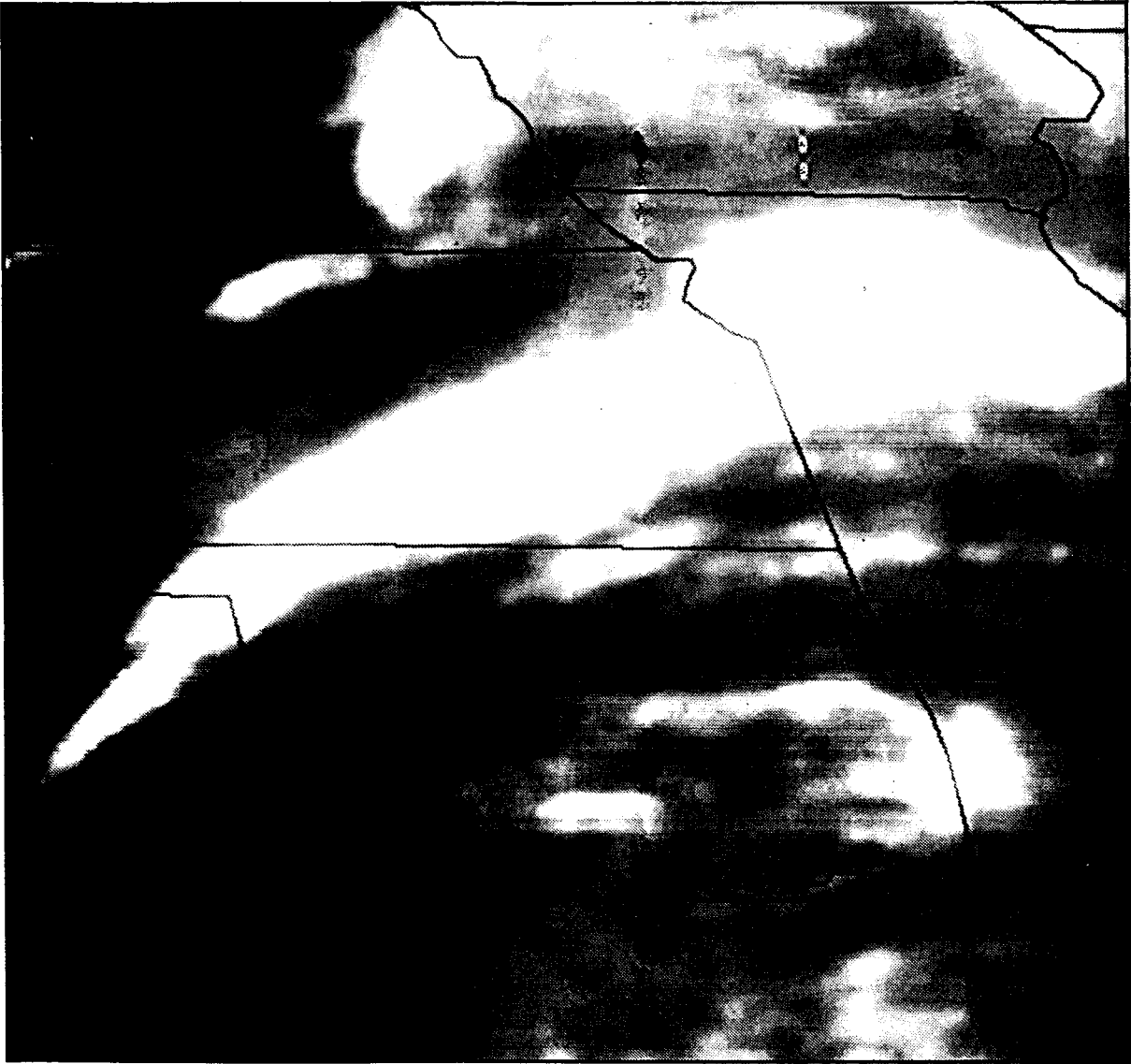


Figure 2-3. Example of IR image magnified to visible resolution

Isolated pixel values which should be adjusted were determined automatically as those which differ by over twenty count values from the preceding value along a scan line. In this case, the data value is replaced by the average of four pixels, namely the two adjacent pixels preceding and following it along the scan line.

2.5 Filtering of Visible Data for Enhancement

An image scene can be processed by applying a digital filter to a specified region surrounding each image picture element. When the pattern of variations in the input data matches the variations in the filter weights, the output value will increase. Thus, for example, with the appropriate choice of weights, the filter can be used to detect regions of the image containing slopes and edges. The use of this type of image as input to the cloud tracking algorithm should have the following advantages:

1. the derivatives tend to minimize sun angle and other brightness effects,
2. they should produce sharper minima in the image differences,
3. directional derivatives provide an independent measurement for each cloud velocity component instead of one single measurement for both components,
4. edge enhancement appears to be a more successful approach, as demonstrated in the registration of Landsat satellite imagery (Nack, 1975).

Several variations of edge detecting filters were applied to the test area.

2.5.1 One Dimensional Gradient or Derivative Filter

In preprocessing the satellite image data for cloud motion calculations, an approach that eliminates brightness trends and detects edges, is a derivative filter. Although this filter has a tendency to magnify noise existing in the original data, it can perform satisfactorily if the original data is smoothed to a certain degree by extending the filter over an n by n picture element array.

The derivative filters have the advantage that they are easy and relatively cost effective to implement and the only choice of variable is the picture element array size or averaging scale, which was chosen as a 5 X 5 pixel area. The derivative output takes on higher or lower values for positive or negative slopes in the data. Thus, the leading edges of clouds are brightened and the trailing edges are darkened, while non-cloud areas remain neutral, as shown in figure 2-4. The cloud motion vectors are determined for each derivative image and then the components merged to form the final cloud motion output.

ORIGINAL PAGE IS
OF POOR QUALITY

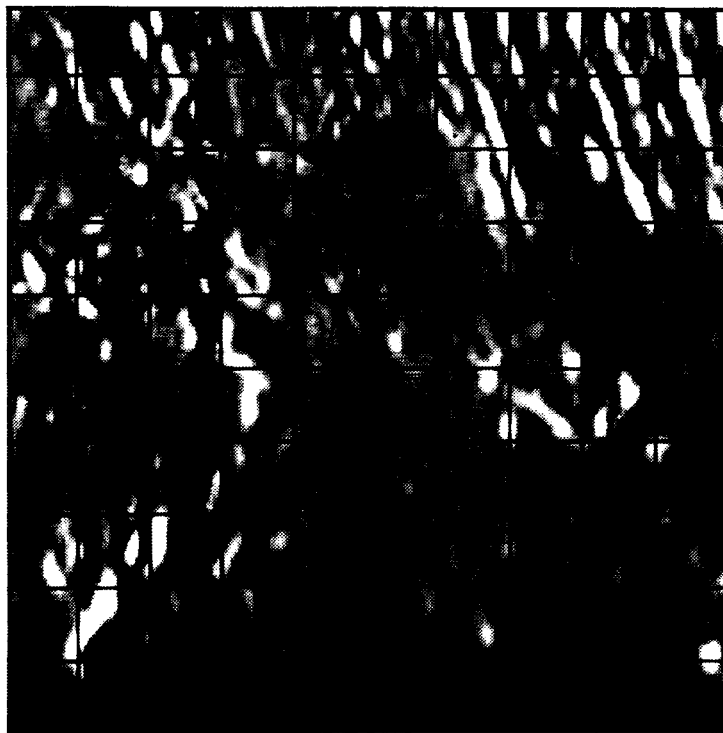
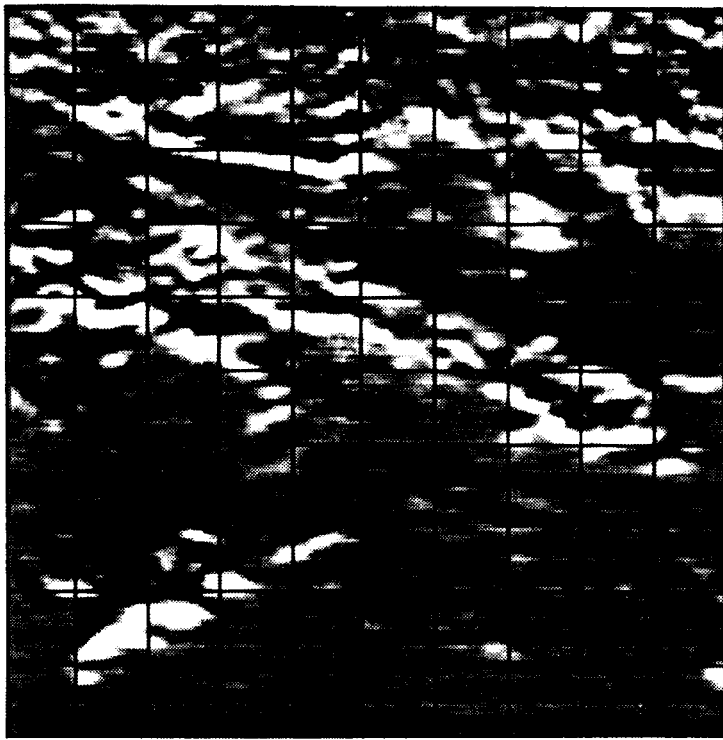


Figure 2-4. Gradient filtered image

2.5.2 Sobel Filter

The use of a nondirectional edge detection filter would eliminate the need for determining the east-west and north-south wind vector components separately. The Sobel operator is widely used, and consists of two gradient filters of size 3 X 3 elements with double weight given to the differences across the central pixel. The filter weights are:

1	2	1	1	0	-1
0	0	0	2	0	-2
-1	-2	-1	1	0	-1

The edge magnitude is the sum of the absolute values of each of the difference terms. The Sobel operator was applied to the test scenes, and an example of a Sobel image is shown in figure 2-5.

2.5.3 Scene Brightness

Since the cloud tracking problem requires the correlation of the brighter objects in the scenes, it should be advantageous to use only the bright areas in the template and search areas. This is accomplished by setting all data values below the mean values of the corresponding areas to zero. If clouds are present, only the clouds will be used, and their edges will be distinct because of the gray level - zero value boundary. Over homogeneous regions where there are no consistently brighter areas, the correlation results should be no better or no worse than those obtained using the raw data. However, an improvement in tracking accuracy would be expected where clouds are present, due to the use of the brighter areas (above the local average brightness) and the generation of edges in the data.

2.5.4 Edge Preserving Filter

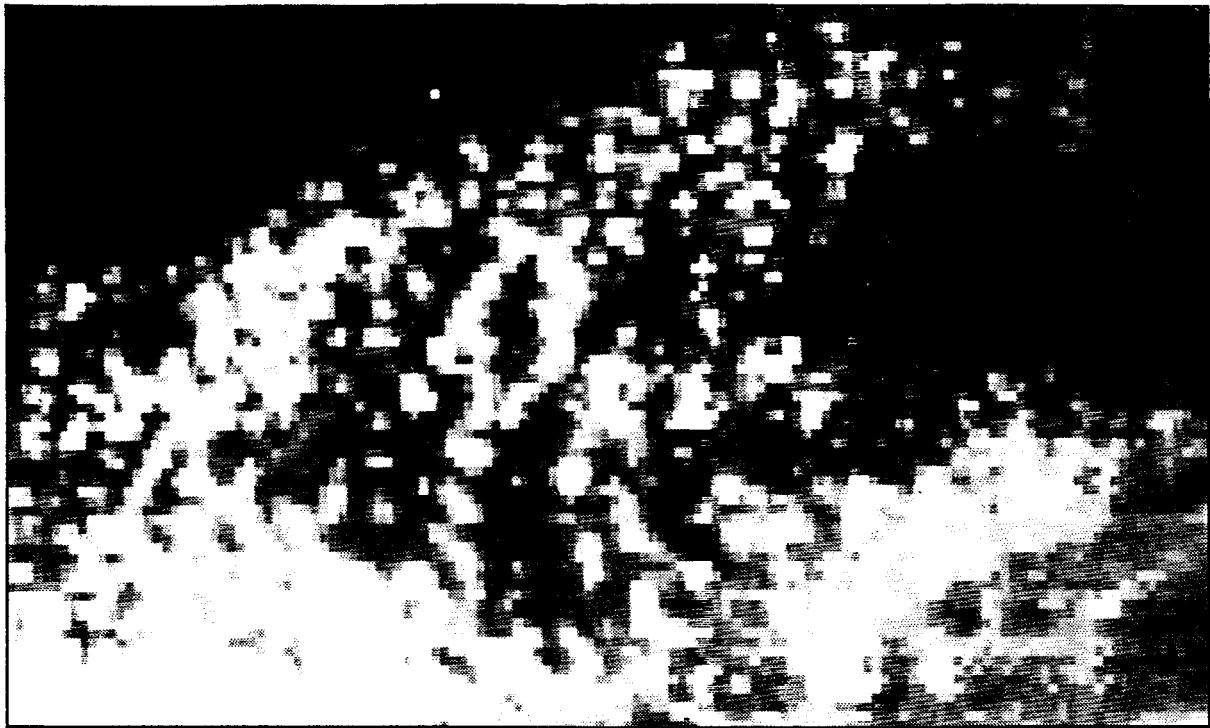
The edge preserving filter which was implemented performs spatial averaging to remove noise, but does not average indiscriminately across edges. In a 3 X 3 matrix surrounding the current pixel, each of the available 2 X 2 sub-matrices is averaged to determine a smoothed value. The current pixel is replaced by the average which is nearest the current value, thus preserving homogeneous regions while rejecting those spatial averages which have been shifted by the inclusion of edges. An example of a filtered image is given in figure 2-6.

ORIGINAL PAGE IS
OF POOR QUALITY

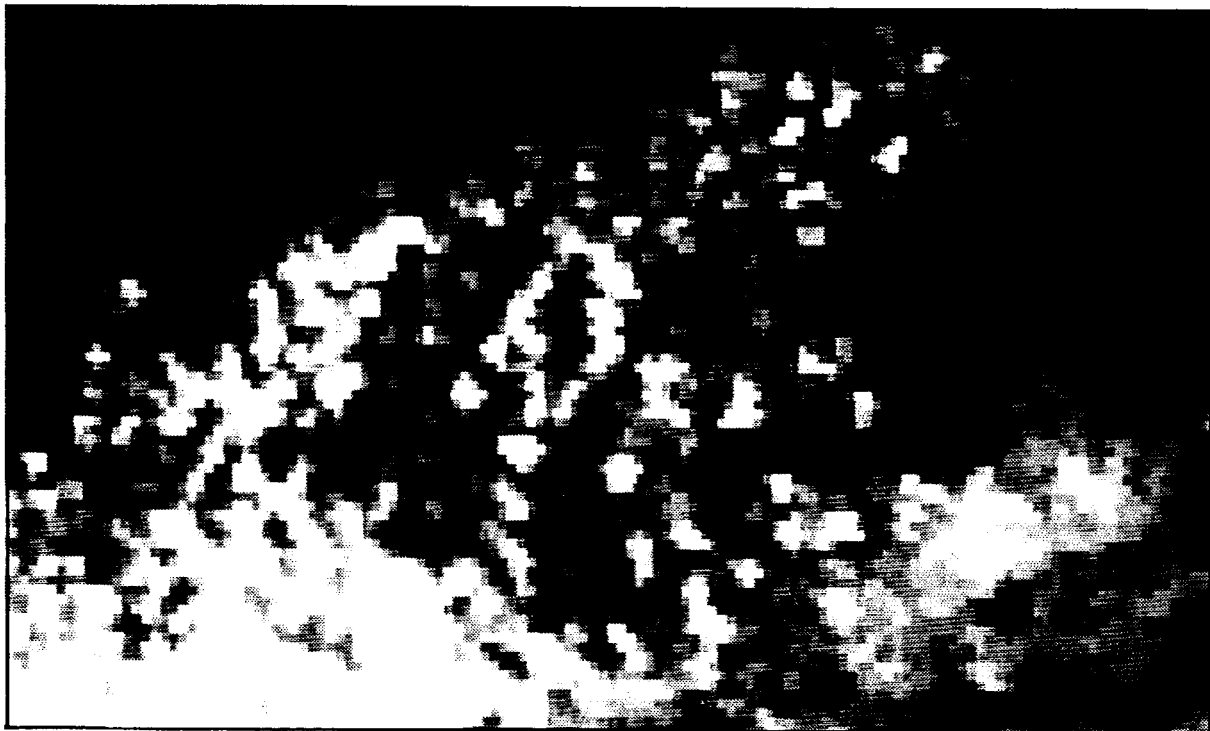


Figure 2-5. Sobel filtered image

ORIGINAL PAGE IS
OF POOR QUALITY



ORIGINAL IMAGE



FILTERED IMAGE

Figure 2-6. Edge Preserving filtered image

3. CLOUD TRACKING TECHNIQUE

The image that was acquired earlier contains numerous image subscenes of cloud patterns called templates, while the image acquired later contains corresponding subscenes called search areas. The template is a square array of picture elements and the spatial location of a template is designated as the template's center picture element (pixel) location in the image. For motion calculations, every template is translated within a search area in the later image and the amount of movement is limited to the maximum pixel translation of a cloud field during the time difference between the two images. A range of cloud displacements may be derived as a 'first guess' from conventional observations of temperature and wind vertical profiles. Since the GOES full resolution pixel spacing is about 900 meters, and the smallest time difference is about 300 seconds, a cloud that has shifted one pixel during the time interval between the acquisition of the images would have a speed of approximately 3 meters per second. Thus, 3 mps is the available speed resolution, improving to 1/2 mps for 30 minute time separation.

The automatic determination of local similarity between cloud templates and all search locations in the search area has traditionally been done using either cross-correlation methods (Leese et al, 1971, Green et al, 1975, Novak and Young, 1977) or pattern recognition (Endlich et al, 1971, Wolf et al, Wolf and Endlich, 1980). However, Barnea and Silverman (1972) describe a different class of digital image registration known as the sequential similarity detection algorithm (SSDA). SSDA involves the simple calculation of a field of "template matching" numbers at every possible translation of the template within the search area. Each such number is the sum of the absolute value differences between every pixel in the template and the corresponding pixel in the search area. This method is unique in that it is computationally fast, requires no normalization of the correlation surface, and, therefore, yields an exact "0" minimum value template match in the ideal nonnormalized registration case.

The quantities obtained from this technique are a minimum template matching number and its position within the search area, which is the template displacement between image scenes. Inter-pixel displacements are estimated by quadratic interpolation over the minimum and its nearest neighbors in two dimensions. Template matching is applied here only to the visible imagery in determining mesoscale wind estimates.

When using the algorithm, there are several decisions to be made that affect the cloud motion results. Three of the decisions concern the choice of candidate template positions and sizes and search area sizes. Because every template has a displacement associated with it, the final decision is to determine which motion vectors are meaningful and related to cloud motion. The majority of the effort has been spent evaluating how to make these decisions.

3.1 Filtering of Visible Image Data

The effects of digital filtering of the visible data were investigated by subjective examination of wind vector plots and by objective examination of the wind vector consistency. Frequency distributions of the displacements and template displacement vectors resulting from the previously discussed preprocessing steps are presented in the following figures.

The results obtained using raw image data as input are shown in figure 3-1. The spurious displacements at ± 8 scan lines seen in the displacements are due to the repeated 8 line sensor pattern in the visible data. Pseudo tracking of this pattern occurs in background areas, but is nearly eliminated when only highly textured regions are tracked.

The merging of components derived from the separate orthogonal derivative images clearly results in a favoring of displacements in the orthogonal directions, as shown by the cross-shaped pattern in the peaks (figure 3-2). Consequently, a compass filter was implemented. In this 3 X 3 pixel filter, the gradient directions are expanded to include the two diagonals, and the derivatives are summed to eliminate the merging of components.

The Sobel filtered results (figure 3-3) show very consistent peaks resulting from the detected edges of clouds. However, there are many incorrect displacements resulting from edge segments which are not sufficiently defined in the two images to be tracked.

The scene brightness technique results (figure 3-4) show less consistency than those from raw data, and hence this technique was eliminated from consideration.

These results indicate that many inconsistent displacements occur when digital filter output is used for tracking, due to background incomplete edges, while edge detected objects are more consistently tracked. It appears that the detail present in the raw data contributes significantly to the tracking accuracy and consequently, a combination of Sobel output with raw data, and edge preserving filtered raw data were tested.

An objective evaluation of results can be made based on the population of motion displacements. Given the assumption that mesoscale cloud fields move in consistent patterns representative of coherent fluid flow structures, only a few values of the displacement vectors should occur. The consistency, as measured by the total number of pixel displacement occurrences is shown in figure 3-5. The raw data and edge preserved raw data yield the most consistent results. The edge preserved results were somewhat improved subjectively, and hence this input imagery was used for subsequent analysis.

ORIGINAL PAGE IS
OF POOR QUALITY

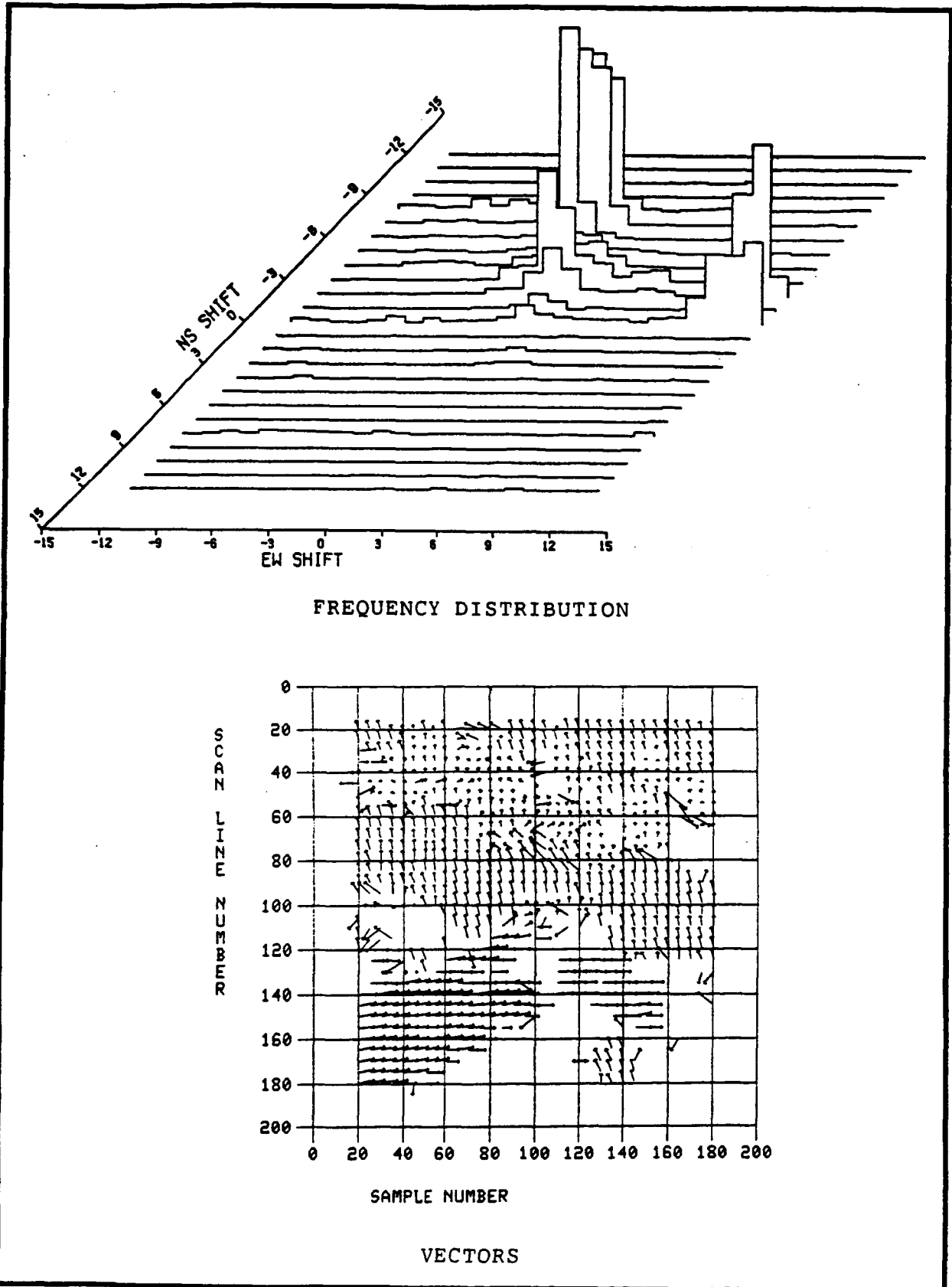


Figure 3-1. Displacement results using raw data input

ORIGINAL PAGE IS
OF POOR QUALITY

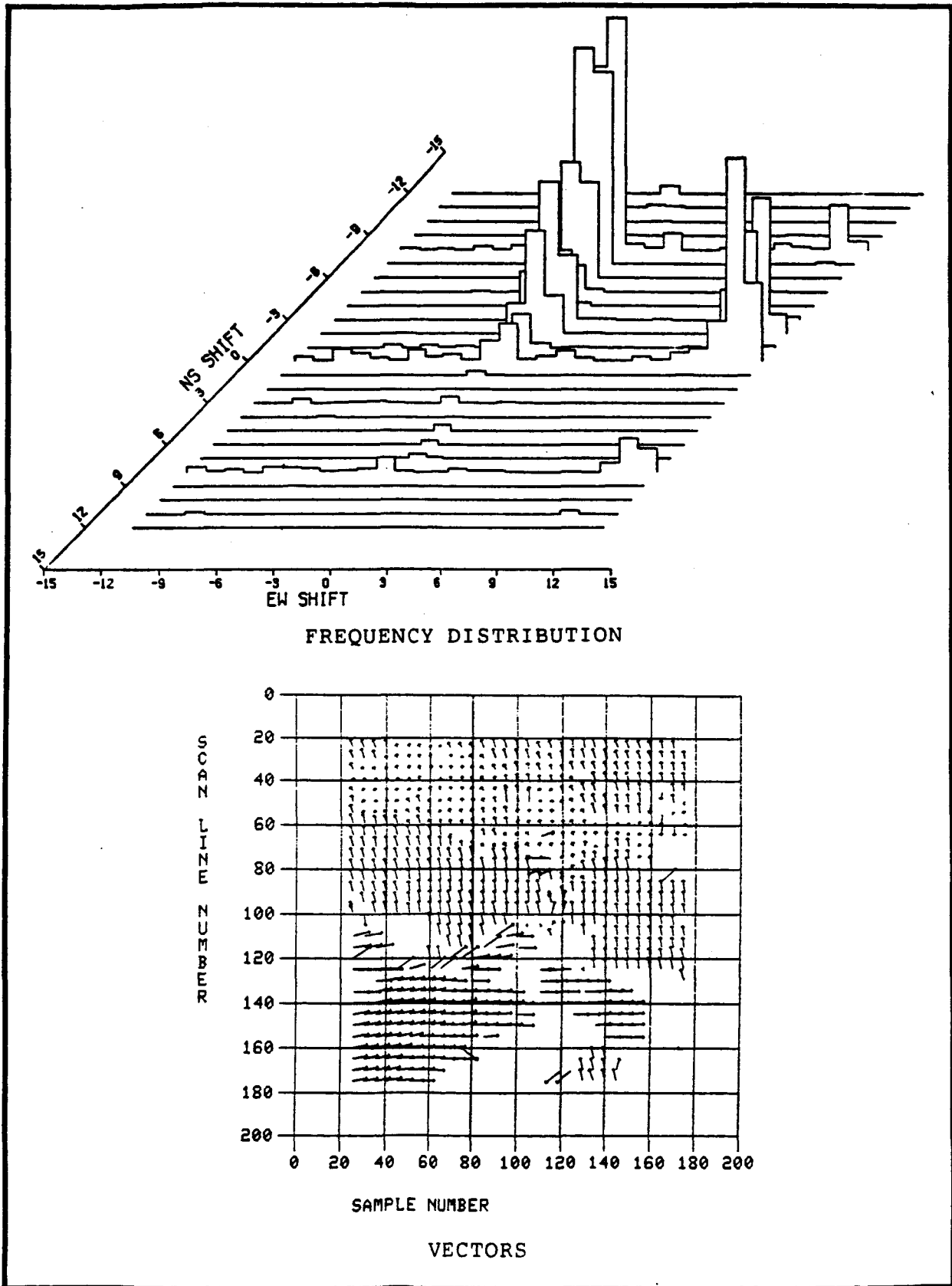


Figure 3-2. Displacement results using gradient filtered input

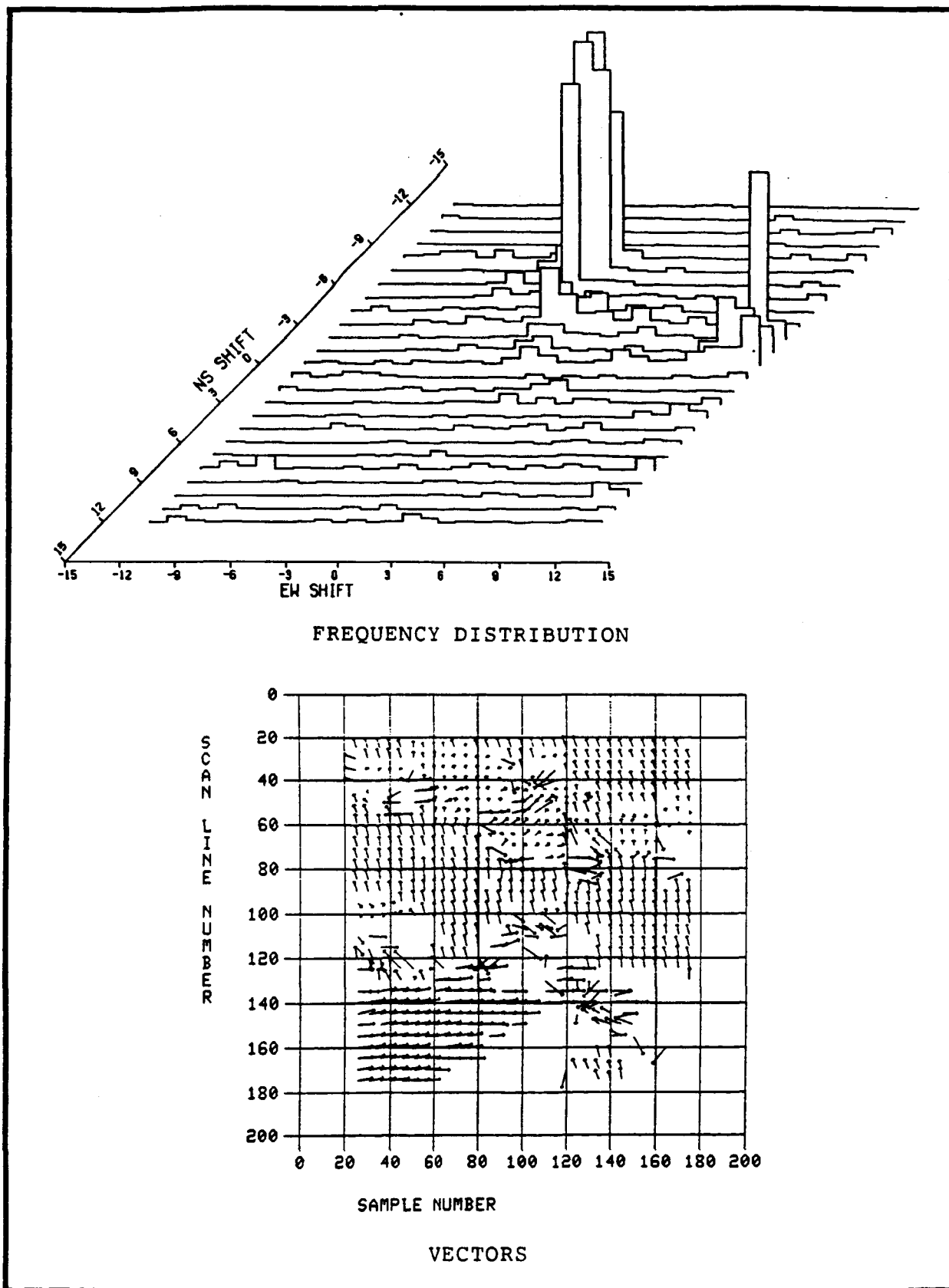


Figure 3-3. Displacement results using Sobel filtered input

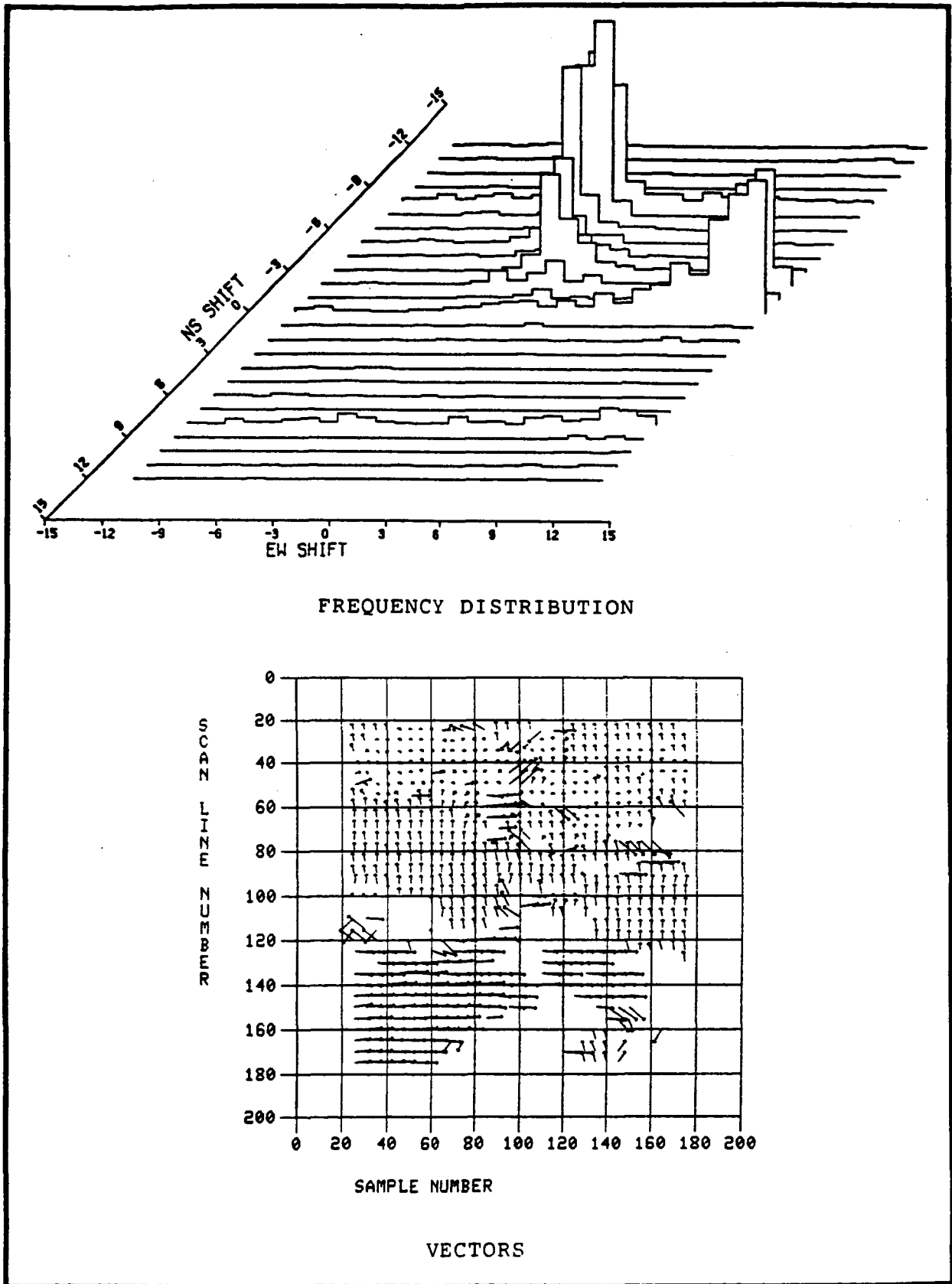


Figure 3-4. Displacement results using scene brightness input

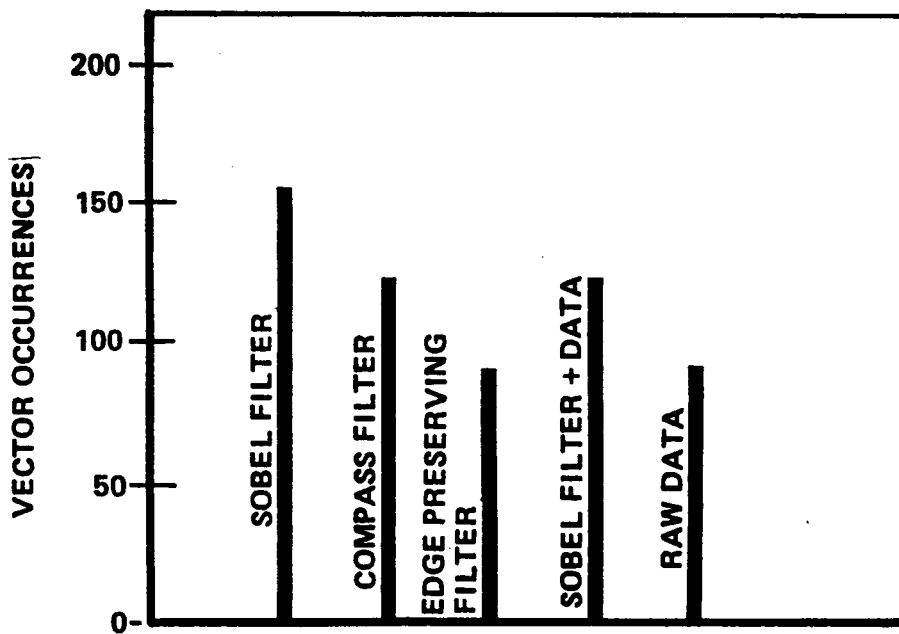


Figure 3-5. Effects of preprocessing on motion vector consistency

3.2 Candidate Cloud Template Positions

Candidate cloud templates were examined every tenth pixel location in each direction so that a maximum mesoscale wind vector spacing of about 10 km results. Motion calculations also incorporated objective procedures for determining image sub-scenes that were 1) representative wind trackers, 2) accurately trackable with automatic techniques, and 3) height assignable.

Image sub-scenes for automatic tracking were chosen by computing infrared and visible standard deviations over the template areas. Experience has shown that visible standard deviations greater than 10 count values 1) assure enough structure for motion tracking, 2) identify most templates with trackable clouds, and 3) eliminate visible sensor banding problems. Infrared standard deviations less than 10 count values 1) eliminate multilevel cloud scenes, thin cirrus, and large and high cloud field edges not moving with the air flow, and 2) ensure that height assignment for the template is possible since the effective variation of black-body temperature over the scene is small and representative of the ambient air temperature.

Figure 3-6 was produced by computing the standard deviation for all possible 13 by 13 templates in the test data, and the center pixel gray scale value of every template was replaced with a gray scale value proportional to that template's standard deviation. The figure shows that large standard deviations tend to occur where there are clouds, and small standard deviations tend to occur where there are no clouds or other bright objects in the ground scene. The distribution of standard deviations was examined and found to be bimodal, suggesting a threshold for eliminating non-cloud (small deviation) displacements. A threshold value of five was applied to the preceding displacement plots and joint histograms.

3.3 Template Size

Over the course of the investigation, a large range of template sizes was examined. At the lower limits of practical template sizes (5 X 5 image pixels), the template does not contain sufficient structural detail to allow matching of the same area in the search image. For small template sizes nearly every possible pixel displacement occurs in a somewhat random manner. Figure 3-7 shows that for a small template size many random displacements occur, while consistent motion is obtained when the template size is increased to 21 X 21 pixels, as shown in figure 3-8.

If the number of displacements that occur is monitored as a function of template size, a situation arises where increasing the template size begins to have a diminishing effect. This situation is illustrated in figure 3-9 and appears to satisfactorily determine a minimum template size, which in this case could be chosen between 25 and 29 pixels.

ORIGINAL PAGE IS
OF POOR QUALITY

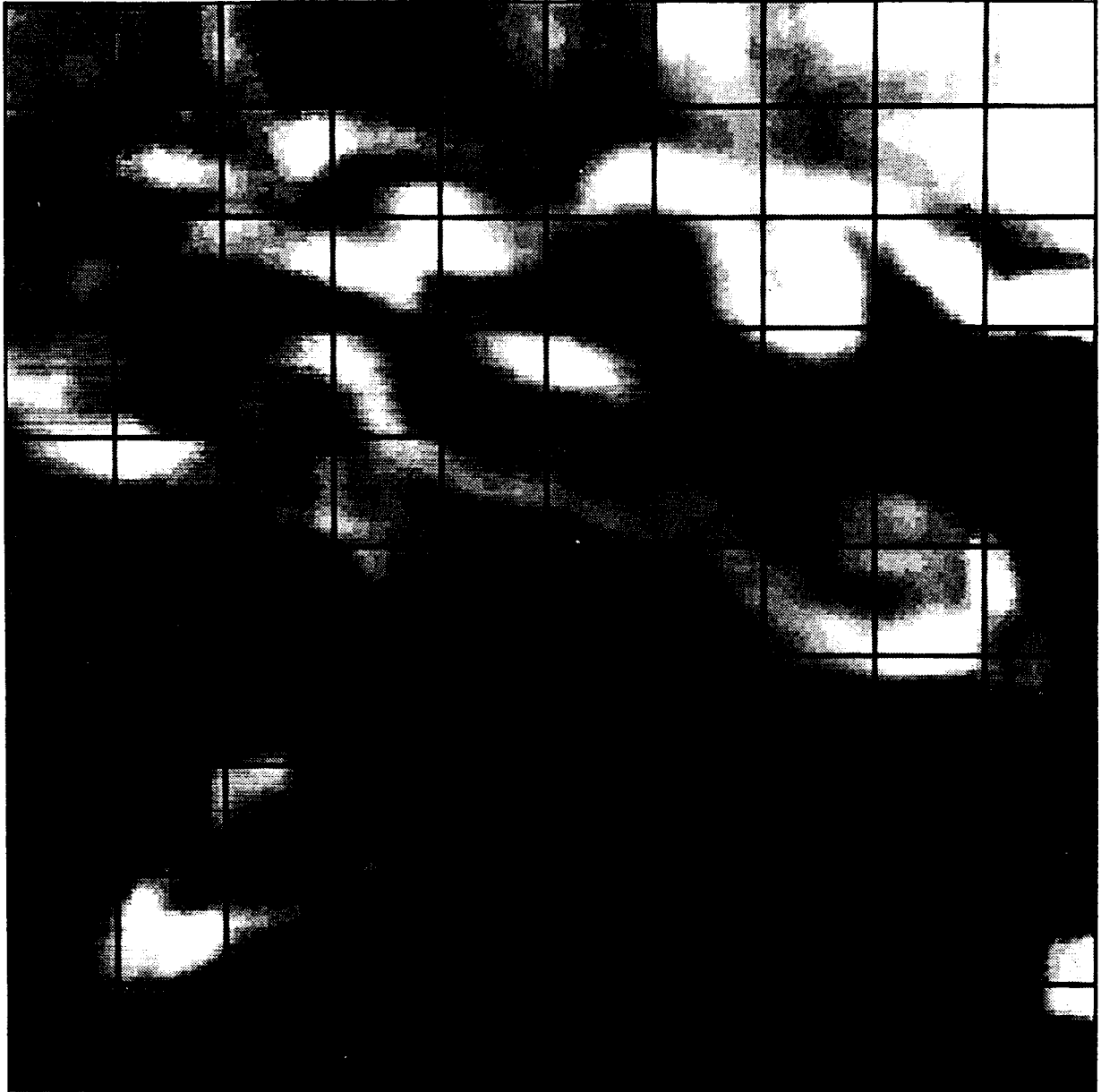


Figure 3-6. Standard deviation image

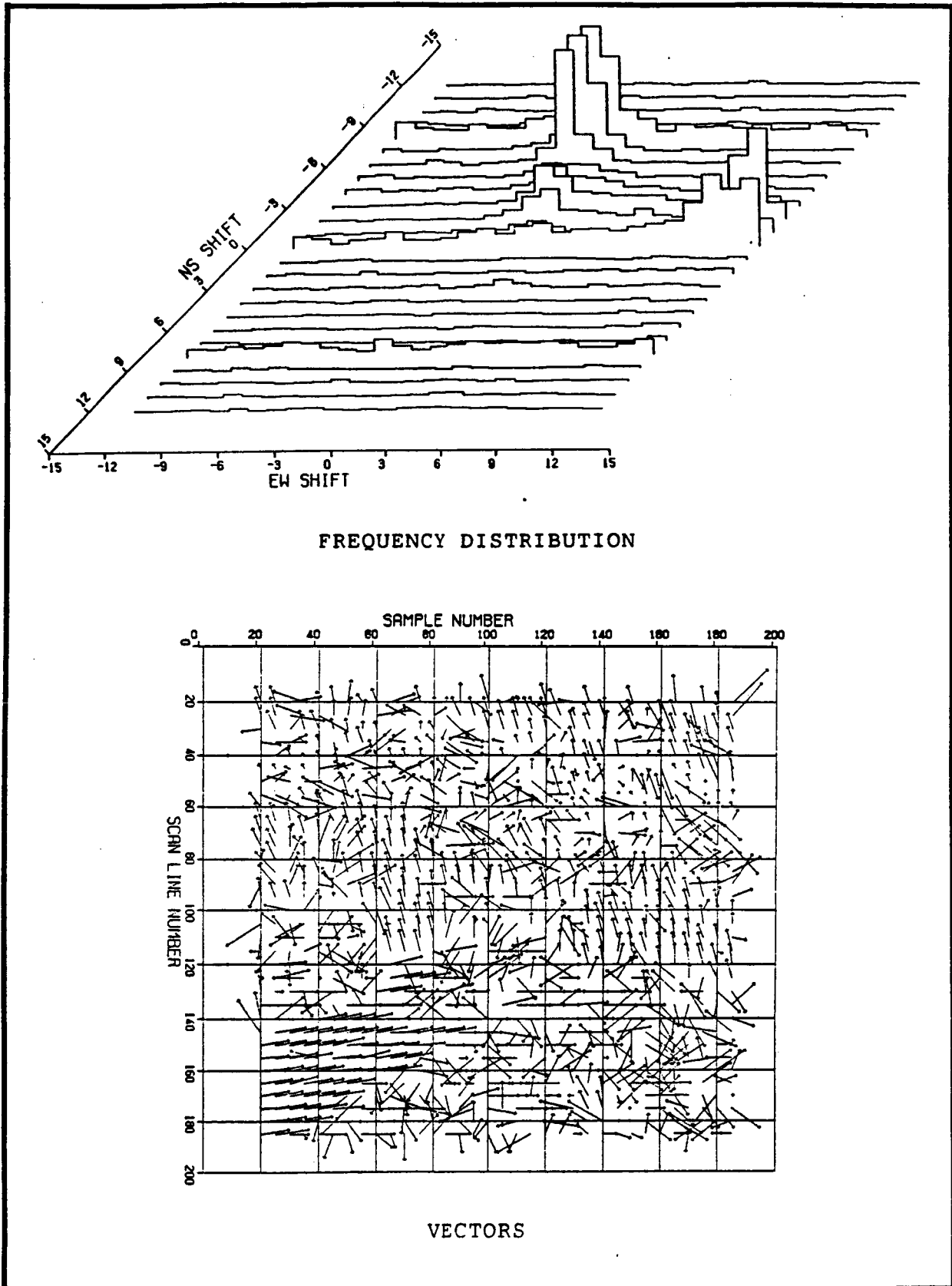


Figure 3-7. Results obtained with a 7 X 7 template

ORIGINAL PAGE IS
OF POOR QUALITY

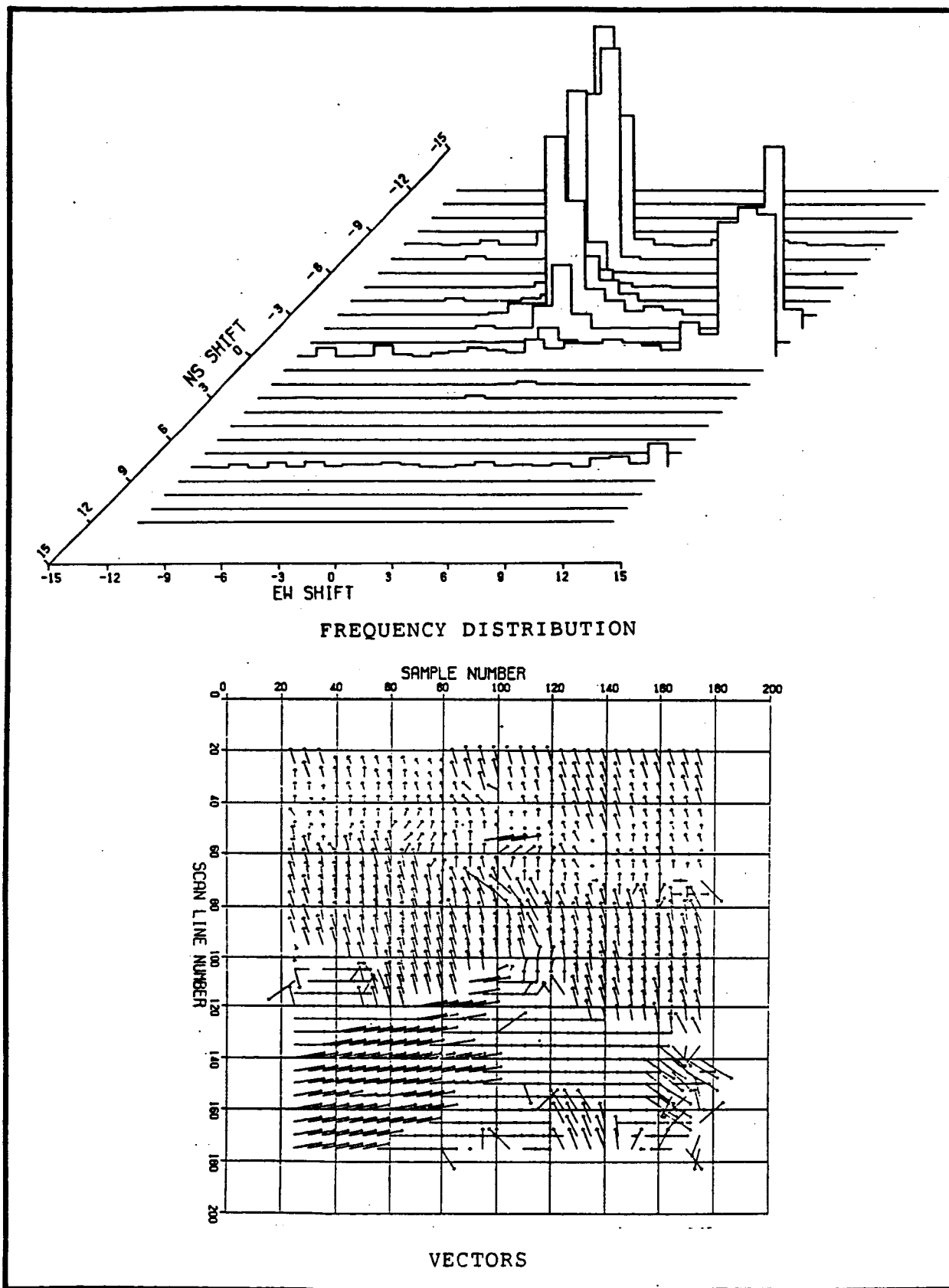


Figure 3-8. Results obtained with a 21 X 21 template

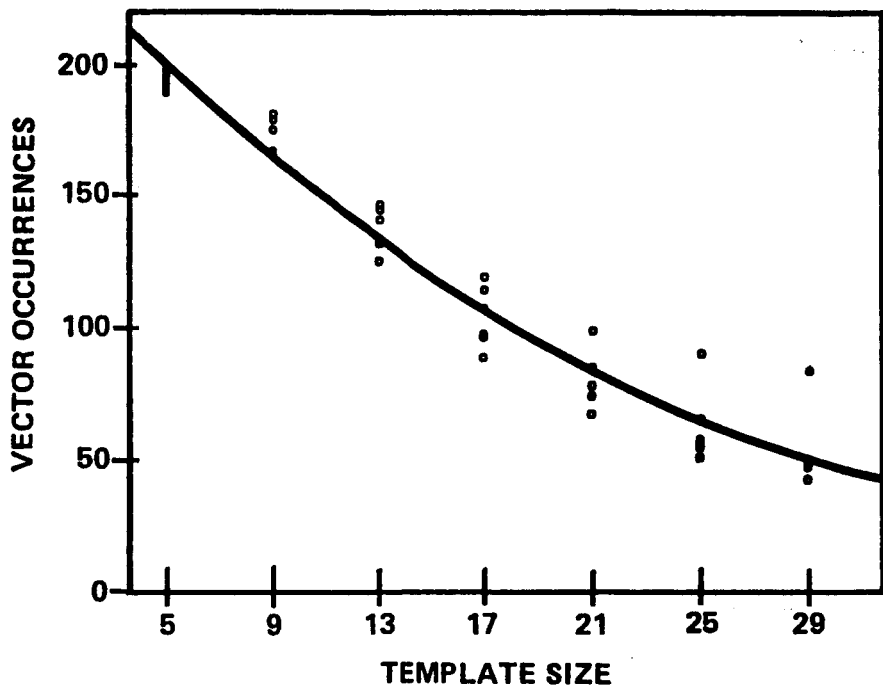


Figure 3-9. Effect of template size on motion vector consistency

The maximum acceptable template size is limited by the possibility of combining separate cloud motions due to the large areas covered. This effect does not appear to be significant for template sizes up to about 50 by 50 pixels. Consequently, calculations of template displacement were performed at each candidate location for template pixel sizes of 25 by 25, 37 by 37, and 49 by 49.

3.4 Search Area Size

Since the template displacement is a function of both wind speed and image-pair separation time, a "first guess" of the actual wind speed is made based upon the height assignment and a vertical wind profile. Profiles of air temperature and wind components vs. pressure heights in gridded form at one degree latitude and longitude increments were generated at ten standard pressure heights from simultaneous radiosonde observations. An example of gridded wind observations is given in figure 3-10.

The height assignment is made at the pressure where the ambient air temperature equals the template temperature. The black-body temperature of the cloud template was computed as the average of the infrared pixel temperatures except when that average was less than 5 degrees C. In this case the coldest pixel was used to compensate for cirrus emissivities much less than 1.0 in portions of the template. Using the infrared template temperature, the height was assigned by interpolation in the vertical temperature profile between the nearest standard pressure heights.

The first guess wind speed is then determined at the assigned height by vertical interpolation between heights and spatial interpolation between grid points. The search area for template matches is determined by a wind speed range about the first guess wind speed. The range is +/- one-half the first guess wind speed, and is restricted to not less than 25 mps and not greater than 40 mps. The search areas are elliptical in shape due to the look angle of the satellite. This control of the search area increases the computational efficiency of the algorithm, and the test area of 1024 by 1024 pixels was used for further analysis.

3.5 Motion Vector Quality Control

Three objective image-processing quality control parameters were developed for use with the SSDA method with the goal of eliminating almost all subjective meteorological editing. The first is the elimination of all SSDA minima that fall on the borders of the search area, since in this case the actual minimum may have been outside the search area. The second and third involve template match quality.

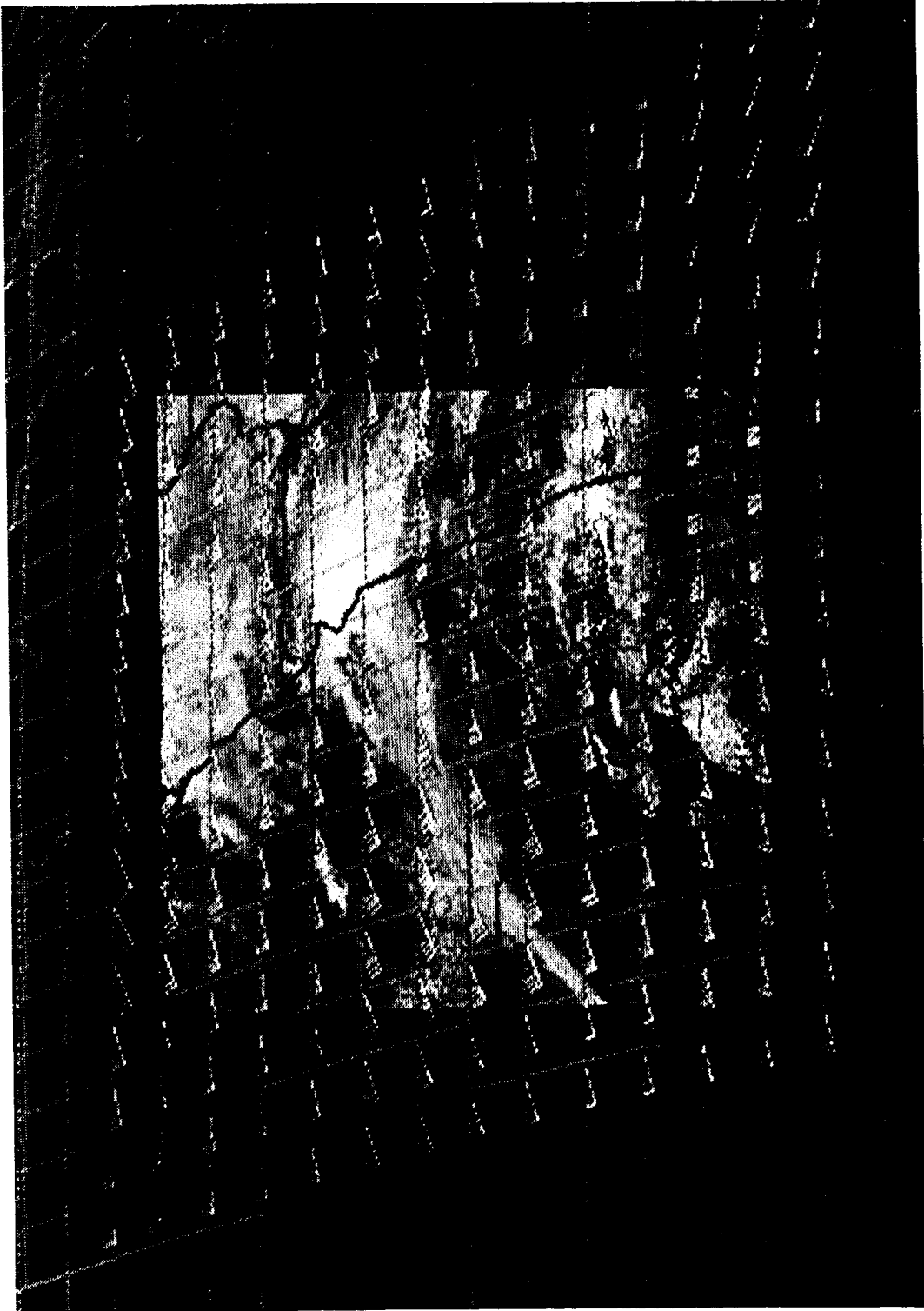


Figure 3-10. Example of wind vectors placed on a grid

The location of the best match between a template and a search area is determined by the structure of a function whose value varies with the template location and the intensity levels of the pixels in the template and search areas. In the technique described here, the function is the total absolute value image difference between the areas on a pixel-by-pixel basis. The best match position occurs when the function reaches its minimum value.

Two characteristics of the image difference function are the average difference over all the search positions tried and the minimum difference found.

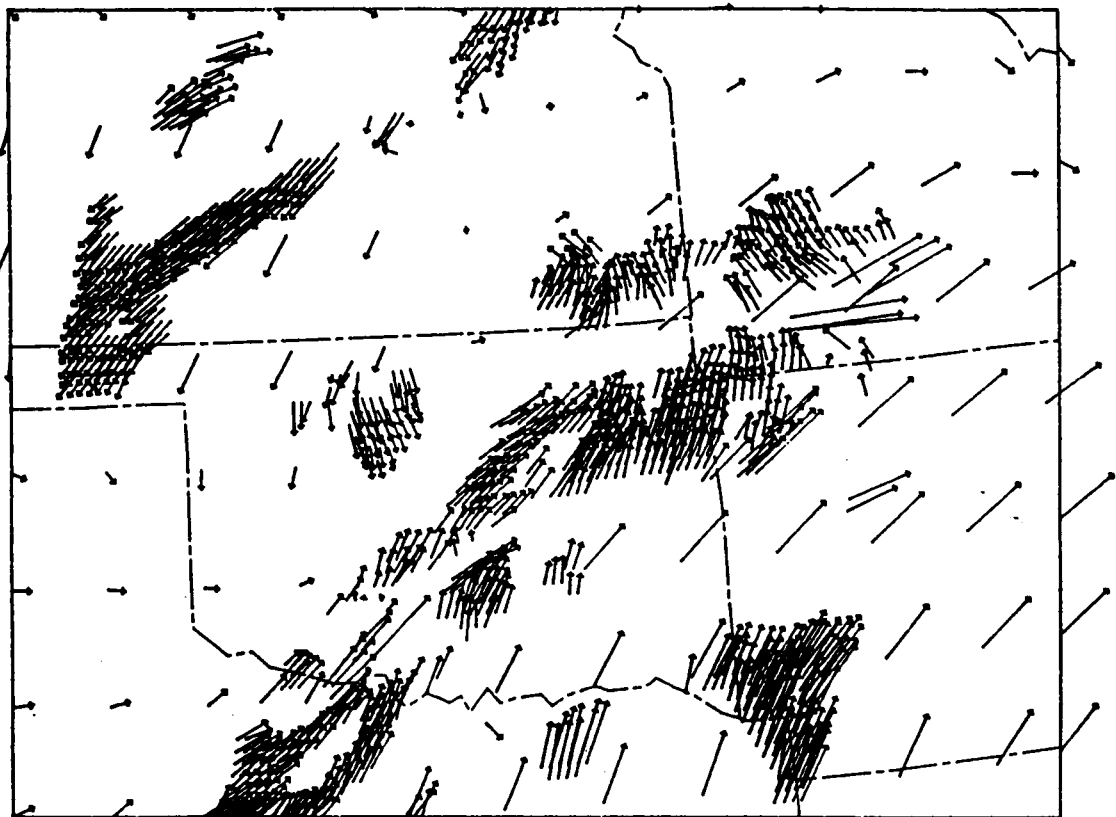
Define $TMQ1 = \text{SSDA mean} / \text{SSDA minimum}$

This template match quality parameter is the ratio of the mean difference to the minimum difference, and as such is a measure of the difference at all the search positions relative to the small value of the difference at match. Successful quality control has consistently been achieved for values of this parameter of 1.6 (ratio 8:5) and above.

An additional measure of quality control is the absence of ambiguous results, which are indicated by a second match position of high quality. If a 3 X 3 element area surrounding the first minimum is eliminated from consideration, the ratio of the secondary and primary minimum differences is a measure of the relative value of the second minimum. The vectors are accepted for values of this parameter of 1.14 (ratio 8:7) and above. With the application of these three quality control parameters fewer than 1% of the wind estimates require meteorological (subjective) editing.

Quality control parameters have been applied to the wind vectors of the large test area covering Oklahoma and Kansas. The low level winds (template temperature above 8 degrees C) are plotted in figure 3-11. For comparison purposes, the equally spaced vectors from the gridded low level radiosonde observations are also shown.

Results obtained from two cases of modified raw data and two cases of digital filter output were also edited by the quality control parameters. The input data types were edge preserving filtered raw data (figure 3-12), Sobel filter output combined with raw data (figure 3-13), Sobel filter output (figure 3-14), and compass filter outputs (figure 3-15). It can be seen that the more consistent results as determined previously by the numbers of unique displacement occurrences (edge preserving filtered data) also contain a greater number of matches which satisfy the quality control tests.



NOTE: THE EQUALLY SPACED VECTORS ARE DERIVED FROM RADIOSONDE OBSERVATIONS

Figure 3-11. Low level satellite derived and RAOB winds

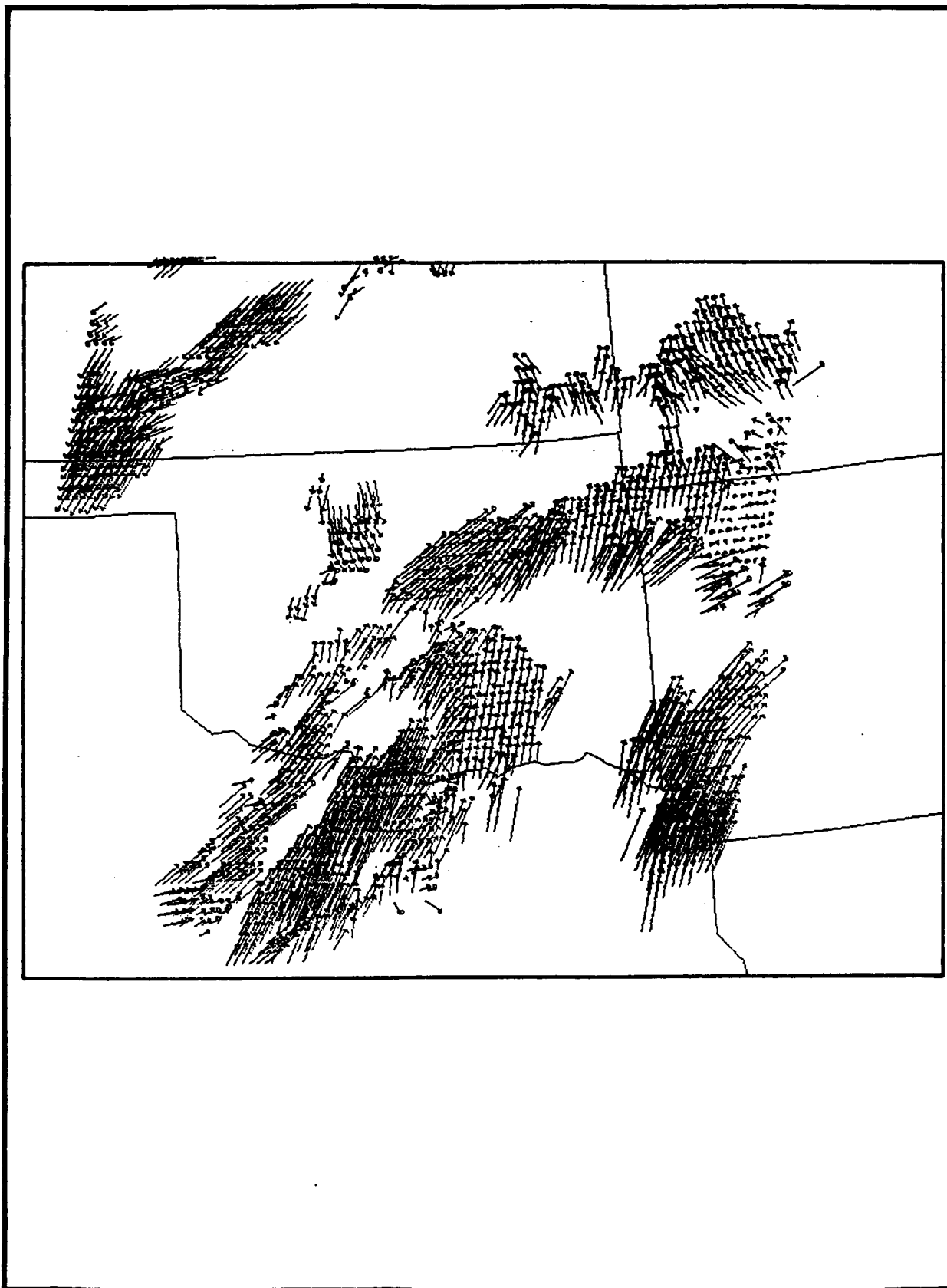


Figure 3-12. Winds from edge preserving filter input

ORIGINAL IMAGE IS
OF POOR QUALITY

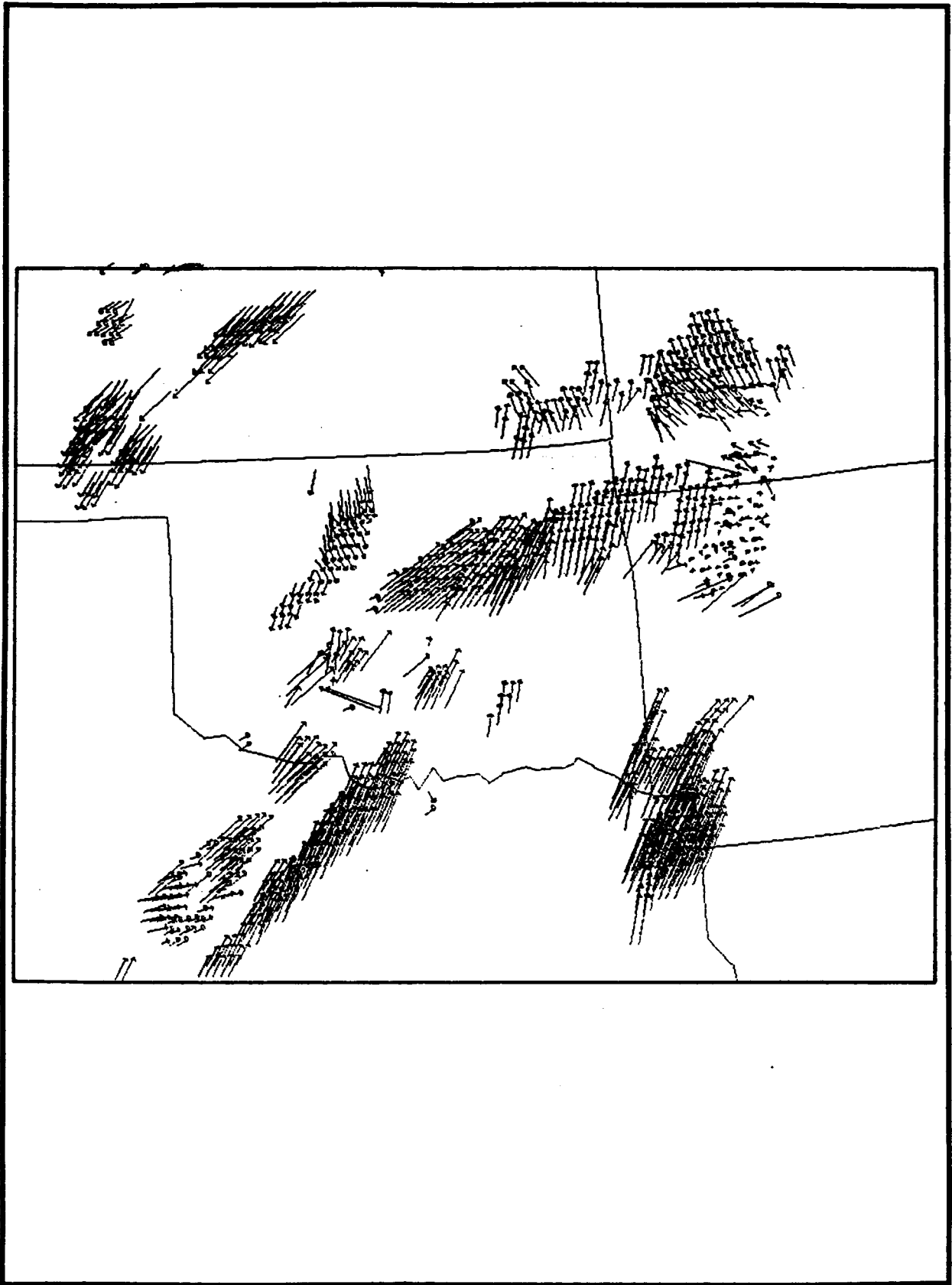


Figure 3-13. Winds from Sobel filter combined with raw data

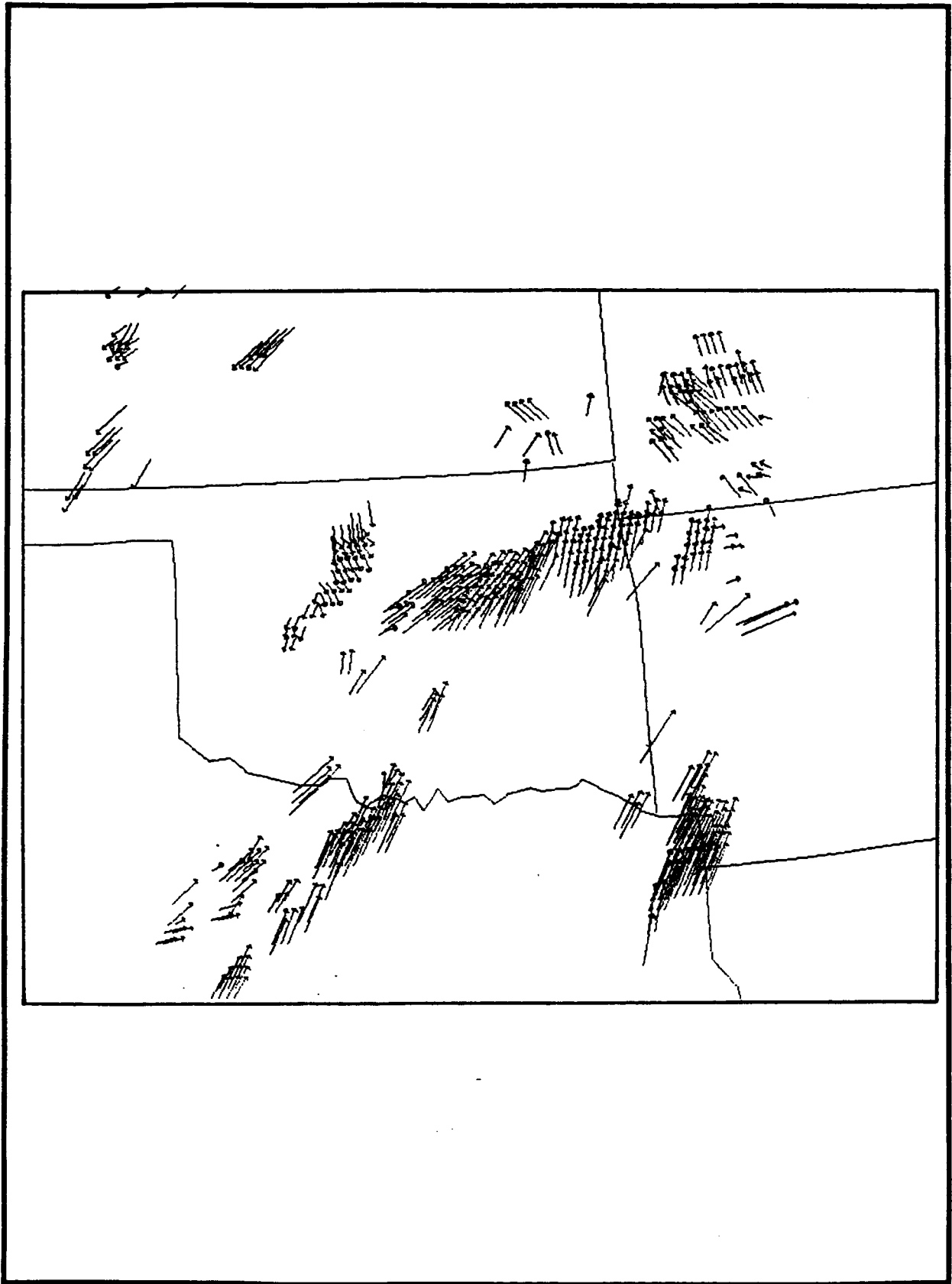


Figure 3-14. Winds from Sobel filter values as input

ORIGINAL PAGE IS
OF POOR QUALITY



Figure 3-15. Winds from compass filter as input

3.6 Height Determination.

An approximate cloud height determination was made from the IR image values converted to temperatures and the RAOB derived temperature profiles. Most of the analysis was done on the low level motions because of the variations at those levels. The upper level cirrus streak in the large test area has a nearly constant higher speed. The upper level vectors are included in figure 3-16.

3.7 Image Acquisition Time Separation.

An increase in image separation time and the corresponding spatial changes in cloud structure result in a decrease in the quality of the template matches. This is shown in figures 3-17 and 3-18 by the decrease in the number of good vectors when the image separation time is increased. However, this effect can be offset by decreasing the spatial resolution of the data through sampling or averaging pixels, as shown in the figures in which the resolution was changed from one km to two km. The improvement arises from the increased areal coverage of the template as the footprint of each pixel is increased.



Figure 3-16. Motion vectors including upper level winds



1 KILOMETER RESOLUTION

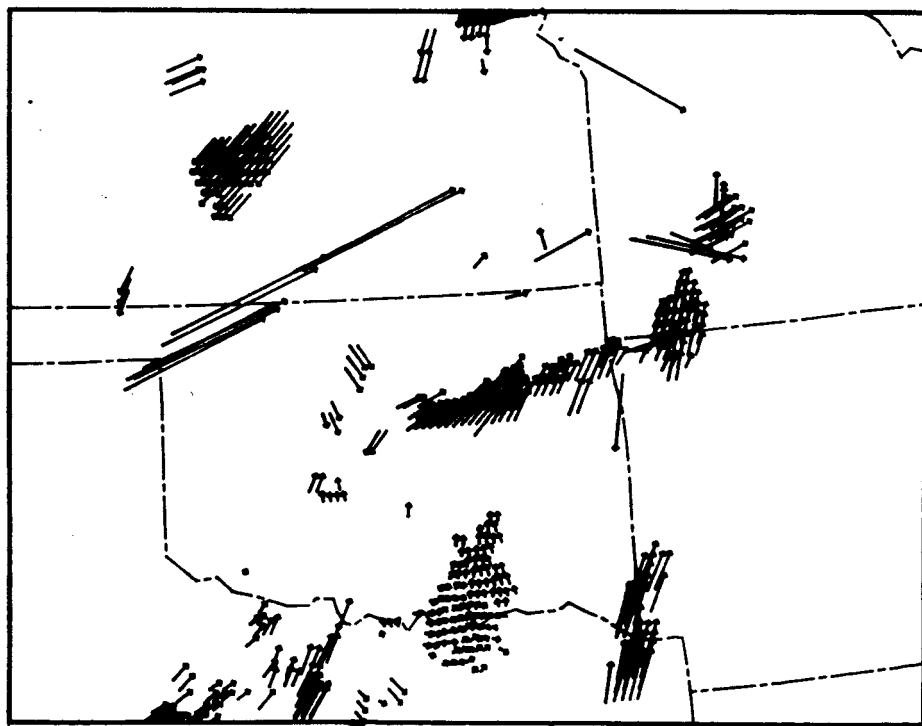


2 KILOMETER RESOLUTION

Figure 3-17. Winds from images separated by 10 minutes



1 KILOMETER RESOLUTION



2 KILOMETER RESOLUTION

Figure 3-18. Winds from images separated by 15 minutes

4. STRUCTURAL AND KINEMATIC ANALYSIS OF AUTOMATED WINDS

4.1 The 24 April 1975 (AVE IV) Case Study

During NASA's Atmospheric Variability Experiment IV (Hill and Turner, 1977) in which special three hour rawinsonde data were taken at NWS sites and 5-min limited-scan VISSR data were recorded, extensive low-level (~850 mb) cumulus and upper-level cirrus cloud fields evolved over the central plains during the pre-thunderstorm period between 1200 and 2100 GMT on 24 April. Severe thunderstorms began developing within the cumulus cloud fields primarily in central and eastern Oklahoma after 2100 GMT and eventually evolved into two historically significant storms: the Neosho, MO tornadic storm and the Wewoka, OK hail storm (see Negri and Vonder Haar, 1980). Five-minute satellite imagery around 2105 and 2130 GMT has previously been used to estimate low-level pre-storm mesoscale moisture convergence and kinematic structure from manually extracted satellite winds computed on NASA's AOIPS computer (Maddox and Vonder Haar, 1979, and Negri and Vonder Haar, 1980). Figure 4-1 shows the satellite imagery onto which are superimposed automated winds.

4.2 Manual and automated wind vectors

An independent McIDAS/WINCO file of manual wind vectors has been produced at the University of Wisconsin for comparison with the automatic winds produced by the new system described herein to allow for both objective and subjective evaluations of the system's performance. Figure 4-2 shows a qualitative comparison between all of the low-level automated cloud winds and the AOIPS and McIDAS/WINCO manually derived winds plotted over a regional-scale area for the 2105 GMT data set. All the techniques provide similar flow structure but the automated vector fields contain nearly six times the number of vectors and somewhat better coverage in areas such as northern Missouri.

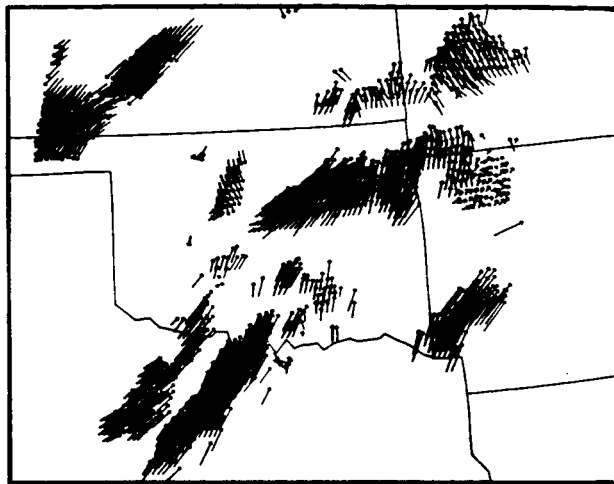
4.3 Mesoscale analysis

Automated low level wind estimates over the region were objectively analyzed onto a 30 km grid using a Barnes procedure for the 2105 through 2130 data. Figure 4-3 shows plots of the resultant low level divergence, for the 2105 GMT data. The strong convergence patterns seen in southwest Oklahoma, northeastern Oklahoma, and Missouri each are associated with severe thunderstorm development during the next three hours.

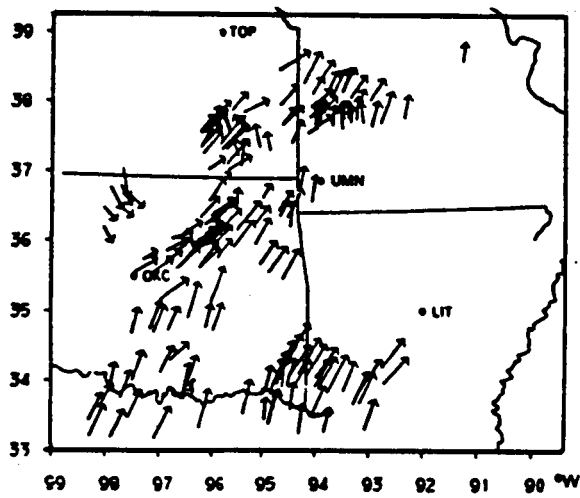
The temporal consistency of mesoscale divergence and vector wind fields is excellent over the 25-minute period, supported primarily by the high density of automated cloud wind vectors surrounding the thunderstorm complexes. Strong centers of meso-B wind convergence associated with 1) a meso-B scale wind-field perturbation in southwestern Oklahoma and, 2) flow-field confluence in northeastern Oklahoma within cumulus cloud-field lines, relate well to the subsequent severe thunderstorm development in these regions.



Figure 4-1. Automated low level winds superimposed on
the visible image



AUTOMATED



MANUAL/AOIPS



MANUAL/MCIDAS

Figure 4-2. Manual and automated wind vectors

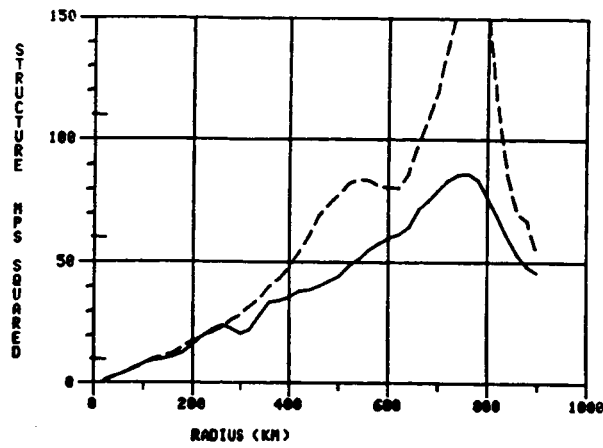


Figure 4-3. Low level divergence computed from automated winds

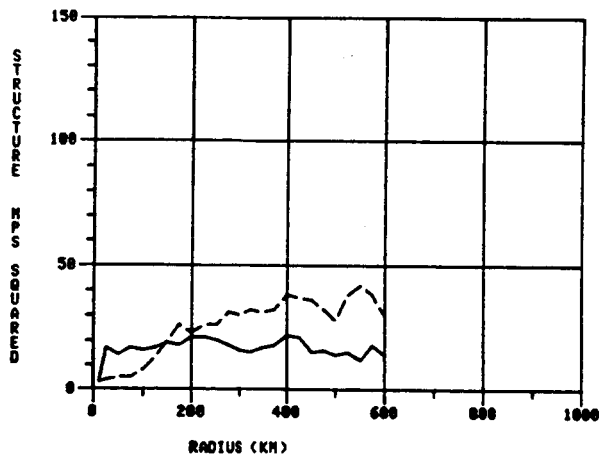
4.4 Structure Functions

Statistical structure functions were computed for u and v components as a quantitative means of comparing both spatial structure and random error estimates of manual vs automated winds. Plots of the wind component structure functions over separation distances extending past 600 km are shown in figure 4-4. The manual vs automated component flow structures are similar in shape but the automated plots are smoother, contain about 30% more spatial variance, and were calculated with many more data pairs.

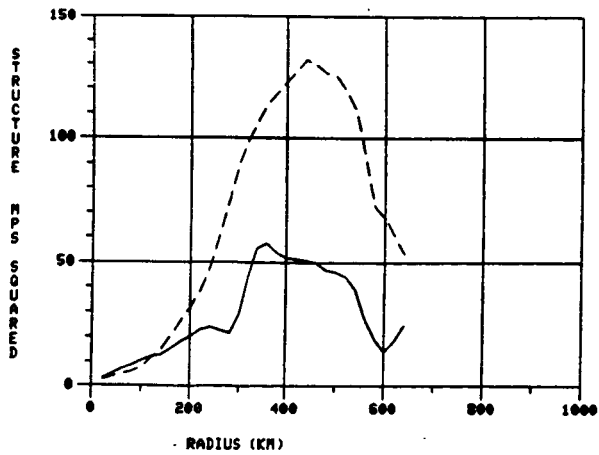
If plots are examined near zero separation distance (the 0-20 km separation bin), a random error estimate can be made since the structure function will approach twice the inherent variance of the measuring system (assuming isotropy, homogeneity, and spatially uncorrelated errors). A random error of approximately 0.86 mps was computed for the 2105 GMT data set, approximately 50% smaller than the 1.75 mps value computed by Maddox and Vonder Haar (1980) using a composite of nine manually-produced cloud-wind data sets.



AUTOMATED



MANUAL/AOIPS



MANUAL/MCIDAS

Figure 4-4. Structure functions of the u and v components (u plotted as solid line)

5. VISSR ATMOSPHERIC SOUNDER (VAS) DATA

The VAS is an extension of the original VISSR imaging capability and includes additional thermal bands for the determination of atmospheric temperature at various altitude layers by spectral selection in the CO₂ absorption bands. Water content is also determined from measurements in the H₂O absorption bands. In addition, the cloud and Earth surface temperature is measured using window-band observations at 3.7 μm and at 11 μm . The standard weighting functions which indicate average pressure heights for the detected radiation in each channel are given in figure 5-1.

The ultimate purpose of the VAS is to increase the understanding of, and ability to predict the behavior of, short-lived weather phenomena such as tropical storms, mid-latitude cyclones, and thunderstorms. In order for the VAS observations to be useful to a forecast and warning system, the observations must be processed and analyzed in a short time compared to the life time of the observed phenomena.

5.1 Preprocessing of VAS Data

VAS imagery at ten-minute intervals was obtained on June 14, 1984. The 6.7 micron water vapor absorption channel (channel 10) was chosen for moisture field tracking. The weighting functions indicate a typical pressure height of 400 mb for radiation received in this channel. The HgCdTe detectors used for this channel produce an output voltage which is related to the input radiance through a gain/offset relation. Unfortunately, there is a drift and variation in the sensor responses which causes striping in the imagery. Additionally, due to the shape of the detectors, scan lines are repeated to preserve the correct aspect ratio of the imagery. As a result, for template displacements across scan lines which are multiples of two scans, the scans are differenced in pairs and artificially low differences result. Because of the inherent lack of structure in this imagery, the tracking algorithm locks onto the striping artifacts. Line template displacements are multiples of two in 97.4% of the cases. Attempts were made to reduce the striping through preprocessing of the data.

5.1.1 Equalization of Means and Variances

For this imagery every fourth scan has similar statistics. The means of the scans for the 1700 GMT scene had values 97.17, 99.13, 95.73, and 100.10, with a range of 4.37 counts. On the assumption that output means and variances arise from sensor offsets and gains, these can be equalized for the whole image and the count values recomputed. Application of this technique reduced the range of scan means to 0.17 counts. A variation on this method is equalization over each four line subset.

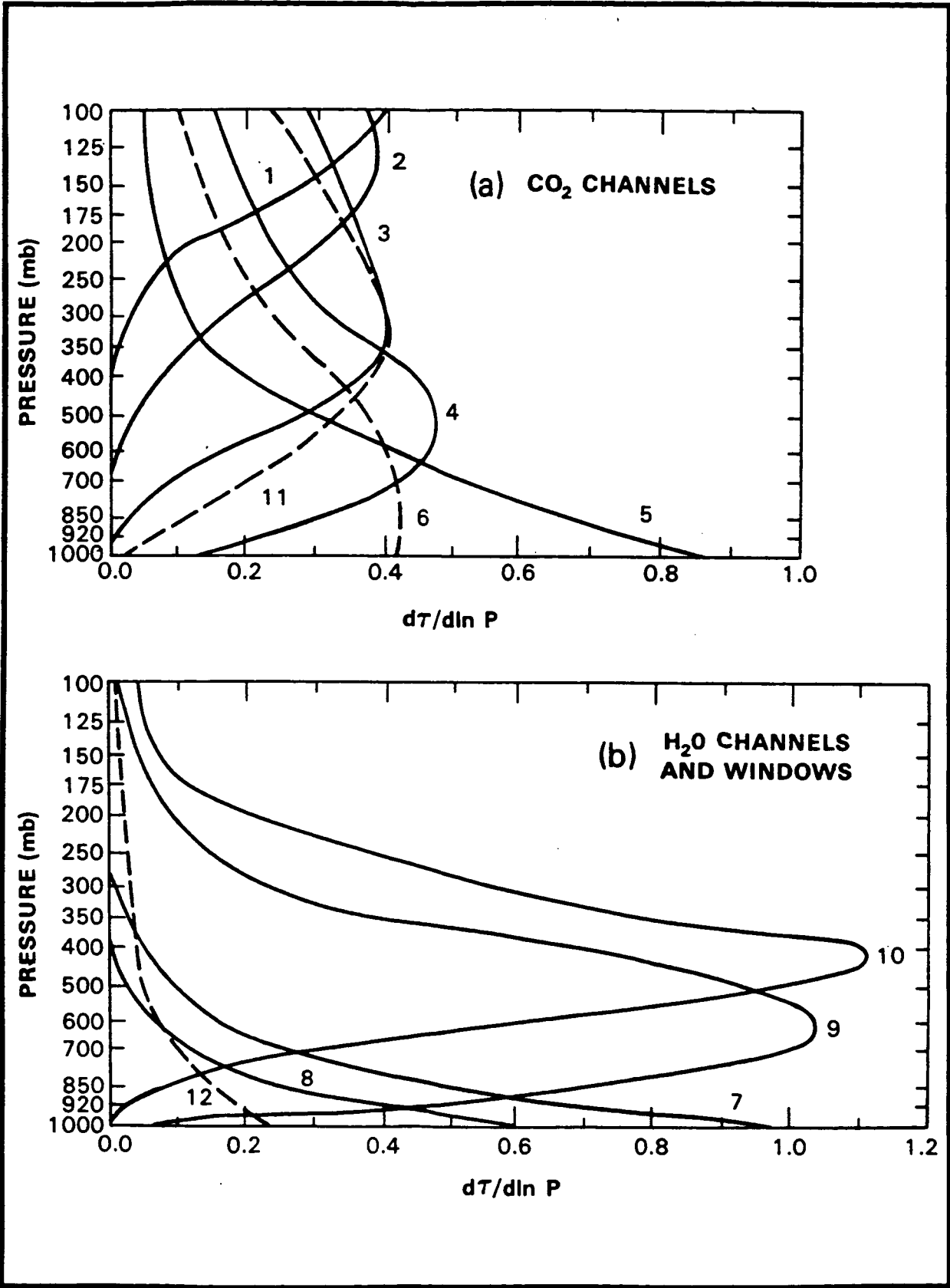


Figure 5-1. Standard VAS weighting functions

5.1.2 Histogram Equalization

The preceding technique assumes linear sensor response curves. This restriction is removed if the actual count distributions are used. If the cumulative histogram of the whole scene is assumed to be the proper nonstriped output, the count values of the individual subscenes are modified so that their distributions match the reference histogram.

5.1.3 Mean Value Filtering

The striping appears as large variations in the mean values of the counts for each scan line. This variation can be removed by filtering over a range of lines and adjusting the line offset to the filtered value. This was done for a nine line range. Small adjustments in mean value are not possible because of the discrete quantization of the count values. However, more exact means were obtained by randomly selecting neighboring count values in the proper proportions to give the correct nonintegral average.

The above methods greatly improved the visual quality of the imagery, with the best technique being histogram equalization. However, the template displacements to stripes remain because of the repetition of the lines in pairs.

5.1.4 Interpolation to Remove Repeated Lines

The repetition of lines was eliminated by performing a linear interpolation between the adjacent line intensity values. The result is a smoothing between the pairs of values, and allows the pixel displacements to take on values with resolution corresponding to each data record, as opposed to multiples of two records. The result of the interpolation on a segment of the image is shown in figure 5-2.

5.2 Water Vapor Winds

The images processed by histogram equalization and interpolation were used as input. Template sizes were increased to account for the slowly changing structure of the imagery. Automated winds are shown in figure 5-3. The gridded RAOB winds at 300 mb are shown for comparison in figure 5-4.

ORIGINAL PAGE IS
OF POOR QUALITY



ORIGINAL IMAGE



INTERPOLATED IMAGE

Figure 5-2. Results of line interpolation on VAS imagery

ORIGINAL PAGE IS
OF POOR QUALITY.

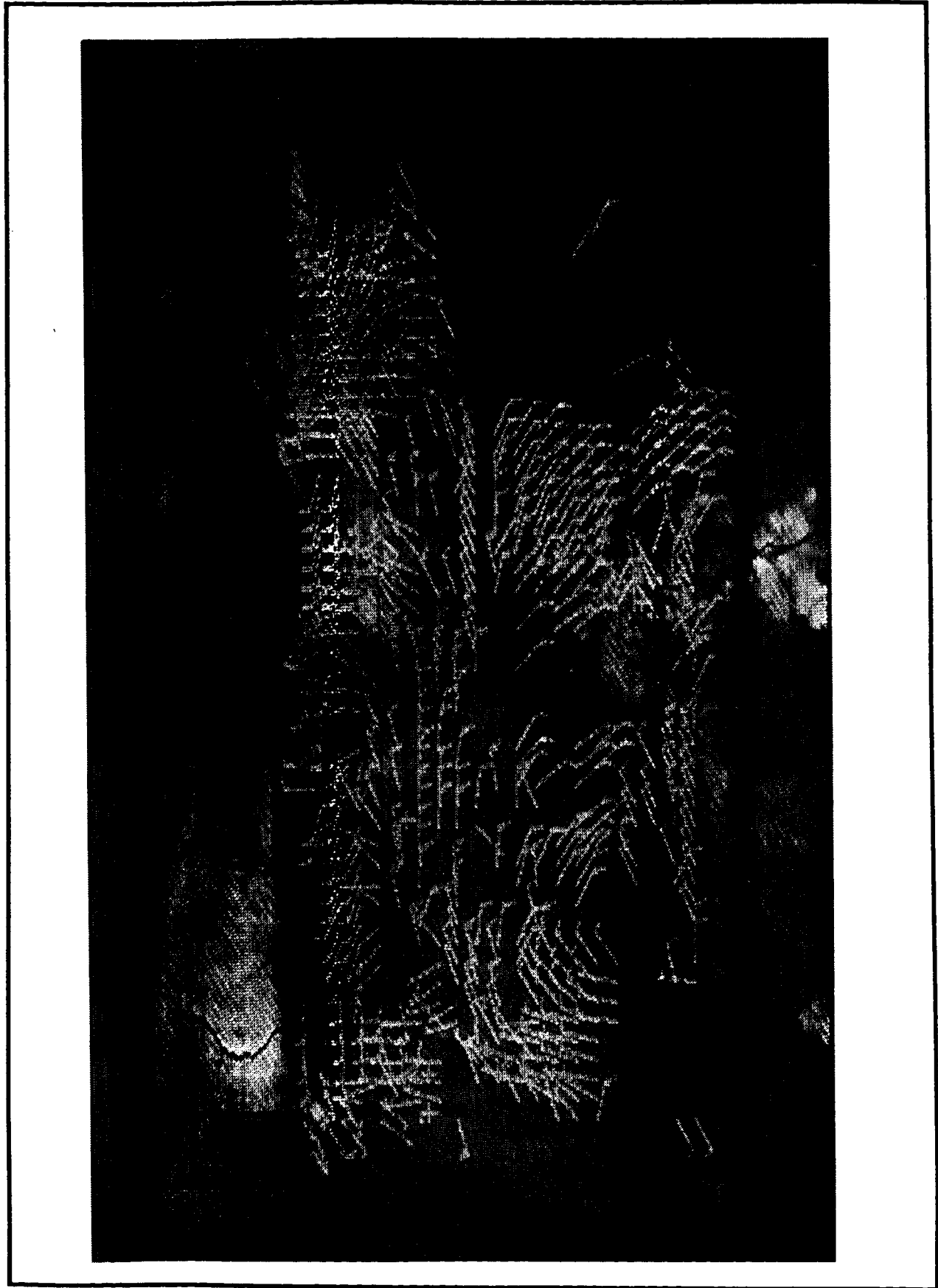


Figure 5-3. Automated water vapor winds superimposed
on VAS imagery



Figure 5-4. Gridded RAOB winds superimposed on VAS imagery

6. CONCLUSIONS

A new automated technique for extracting mesoscale wind fields from GOES visible/infrared satellite imagery has been developed. Quality control parameters were defined to allow objective editing of the wind fields. The system can produce equivalent or superior cloud wind estimates compared to the time-consuming manual methods used on various interactive meteorological processing systems. Analysis of automated mesoscale cloud wind for a test case yields an estimated random error value one meter per second and produces both regional and mesoscale vector wind-field structure and divergence patterns that are consistent in time and highly correlated with subsequent severe thunderstorm development.

7. REFERENCES

- Barnea, D. I., and H. F. Silverman, 1972: A Class of Algorithms for Fast Digital Image Registration. IEEE Trans. on Computers, C-21, 179-186.
- Endlich, R. M., D. E. Wolf, D. J. Hall, and A. E. Brain, 1971: Use of a Pattern Recognition Technique for Determining Cloud Motions from Sequences of Satellite Photographs. J. Appl. Meteor. 10, 105-117.
- Green, R., G. Hughes, C. Novak, and R. Schertz, 1975: The Automatic Extraction of Wind Estimates from VISSSR Data. Central Processing and Analysis of Geostationary Satellite Data, NOAA Technical Memorandum NESS-64, 94-110.
- Hill, K., and R. E. Turner, 1977: NASA's Atmospheric Variability Experiments (AVE). Bull. Amer. Meteor. Soc. 58, 170-172.
- Hubert, Lester F., 1979: Wind Derivation from Geostationary Satellites. Quantitative Meteorological Data from Satellites, World Meteor. Organization Technical Note No. 66, ed. Jay S. Winston, 33-59.
- Leese, John A., Charles S. Novak, and Bruce B. Clark, 1971: An Automated Technique for obtaining Cloud Motion from Geosynchronous Satellite data using Cross Correlation, J. Appl. Meteor. 10, 118-132.
- Maddox, R. A., and T. H. Vonder Haar, 1979: Covariance Analysis of Satellite Derived Mesoscale Wind Fields. J. Appl. Meteor. 18, 1327-1334.
- Menzel, W. P., W. L. Smith, and T. R. Stewart, 1983: Improved Cloud Motion Wind Vector and Altitude Assignment using VAS. J. Appl. Meteor. 22, 377-384.
- Nack, M. L., 1975: Temporal Registration of Multispectral Digital Satellite Images using their Edge Images, Proc. AAS/AIAA Astrodynamics Specialist Conf.
- Negri, A. J. and T. H. Vonder Haar, 1980: Moisture Convergence using Satellite-derived Wind Fields: a Severe Local Storm Case Study. Monthly Weather Review 108, 1170-1182.
- Novak, C., and M. Young, 1977: The Operational Processing of Wind Estimates from Cloud Motions: Past, Present and Future. Proc. Eleventh Intl. Symposium on Remote Sensing of the Environment, Ann Arbor, Michigan, 1589-1598.
- Wylie, Don, 1980, Space Science and Engineering Center, University of Wisconsin, Private Communication.